Rubidium resonant squeezed light from a diode-pumped optical-parametric oscillator

Ana Predojević

April 6, 2009

Memoria de la tesis presentada por Ana Predojević para optar al grado de Doctor, mencion Doctor Europeo

Director de la tesis: Dr. Morgan W. Mitchell

Tutor: Dr. Jordi Boronat Medico

ICFO-Institut de Ciències Fotòtoniques & Departement de Física Aplicada y Simulación en Ciencias de Universidad Politècnica de Catalunya

"No esperéis demasiado del fin del mundo"
Stanislaw J. Lec, Aforyzmy, Fraszki, Kraków,
Wydawnictwo, Literackie, 1977,
"Myśli Nieuczesane"

Agradecimientos

El apartado de agradecimientos de una tesis es complicado de escribir, dado que no sólo es la sección que todo el mundo lee, sino que muchas veces es la única parte leída. No estoy segura de por dónde empezar la larga lista de gente a la que, por un motivo u otro, tengo que dar las gracias pero por algún punto debo hacerlo y espero me perdonen los que creerán me he equivocado en el "ranking". No fue a propósito.

Sin duda el primer y principal agradecimiento va dirigido a mis compañeros. A Núria, que aunque siempre rezagada a la hora de comer me enseñó a hablar el idioma con el que escribo estas líneas; a Xavier, que siempre me ha sabido ayudar a mantener el ánimo; al "Consejo de Tres" (José Manuel y Susana), que me acogieron mientras no disponía de techo y me ayudaron a conocer "la España profunda"; a Iñes la valiente. También quiero dar las gracias a todos los que los ICFOnians llaman "la administración": a Zsuzsi, a Maria José, a Ferran (siempre en contra de todo), a Yolanda, a Montse, a Gemma... porque sin su ayuda y apoyo no hubiera sido posible hacer un nuevo experimento y un nuevo laboratorio en tan poco tiempo. A Mari Carmen, por cuidar de mis flores cada vez que he permanecido fuera. También merece ser agradecido el personal de los talleres (José Carlos encabezando la larga lista) que me ayudó muchísimo a llevar a cabo unos proyectos complicadísimos (algunas cosas las hicieron un poco a regañadientes, pero sin quejarse en exceso); a la gente amable de IT que siempre ha tenido tiempo para responder mis preguntas aunque muchas fueron muy tontas.

En segundo lugar debo mencionar a mi supervisor, Morgan Mitchell (también conocido como Mitchell Morgan), al que a veces tuve que dar algún pequeño empujón para lograr terminar las cosas a tiempo – se quejó moderadamente, pero sobrevivió. También, (lo escribiré en inglés para que me entienda) *I would like to thank Eugene Polzik who made all this possible.* Mario (*més català* que el *pa amb tomàquet*), Herbert, Marco, Zehui, Marcin, Florian y Ale integraron el grupo de investigación al que pertenecí y quiero darles las gracias por las experiencias que me regalaron y que no serán olvidadas ni mañana ni pasado.

Lluis Torner y Dolors Mateu, como director y gerente del ICFO respectivamente, fueron piezas imprescindibles para llevar a cabo mi tesis doctoral y no puedo hacer otra cosa que mencionar sus nombres como muestra de gratitud hacia ellos y hacia la institución que representan. Por otro lado, todos los investigadores en el ICFO encontrados, sus vidas, sus estímulos y sus experiencias conforman un bagaje importante para mí: Caitriona, Petru, Ian, Dobryna, Srdjan, Matteo, Carsten, Felix, Marc, Tristán y los demás comunistas del pasillo rojo en su conjunto permanecerán bien arriba en esta lista.

En relación con mi familia voy a empezar nombrando a mi abuela que, a

pesar de sus 82 años, sigue siendo la más lista de todos. Señalar a mi madre, que nunca me perdonó lo de no hacerme dentista. A mi padre también, que siempre respondería a cada tontería mía con la misma frase: "pues si te hace feliz...". A Zlatko mi "šudili", mi alma gemela, por su amistad eterna y por apoyarme en todo a pesar de la distancia, muchas gracias.

Quiero hacer mención a todos los hombres que durante este periodo de tiempo han pedido mi mano y he tenido que rechazar porque mi madre no los hubiera aceptado por pobres (es una broma, no suelo escuchar a nadie). También al chico desconocido que desde el portal de mi casa y durante largas noches me ha acompañado con su bongo, cuyo sonido insistente me ha acostumbrado a dormir en cualquiera situación y ha hecho que alargase mis horas de trabajo durante este proceso de enseñanza. Quiero también que queden aquí unas palabras relativas al barrio barcelonés del Raval, en el que he vivido rodeada de inmuebles resquebrajados, como el mío, y en el que he compartido experiencias insólitas con muchos miembros del submundo que se esconde en él: el vendedor de butano pakistaní que cada Sábado tuvo a bien despertarme con sus gritos, a su compañero gitano que llegaba posteriormente con su música y sus potentes altavoces, a Doña María, que me suministró quesos y parte de su alma en su tienda Rosa d'Abril, etc.

Seguidamente no puedo hacer otra cosa que manifestar mi agradecimiento a la Generalitat y a los ciudadanos de Cataluña (también conocidos como "la gente normal"), con los impuestos de los cuales mi tesis pudo salir adelante. Queda aquí por escrito mi compromiso de permanecer siempre como embajadora fiel a este pueblo, vaya donde vaya, elogiando sus virtudes y perdonando sus pecados.

Para finalizar, y de entre lo mucho que me llevo de este país, también apuntar la existencia de un ser para mi muy especial, Markus, que me ayudó muchísimo, aguantando carros y carretas.

Agraïments

L'apartat d'agraïments d'una tesi és difícil d'escriure atès que no sols és la secció que tot el món llegeix, sinó que moltes vegades és l'única part llegida. No estic conveçuda de per on començar la llarga llista de gent a la que, per un o altre motiu, he de donar les gràcies però per algun punt he de fer-ho i espero que em perdonin els que creuran que m'he equivocat en el "rànking". No ha estat exprés.

Sens dubte el primer i principal agraïment va dirigit als meus companys. A la Núria, que tot i arribar sempre tard a l'hora de dinar m'ha ensenyat la llengua amb la que escric aquestes línies; al Xavier, que sempre ha sabut mantenir-me animada; al "Consejo de Tres" (el José Manuel i la Susana), que m'acolliren mentre no disposava d'un sostre i m'ajudaren a conèixer "la España profunda", a la Iñes la velenta. També vull donar les gràcies a tots els que els ICFOnians anomenen "l'administració": a la Zsuzsi, a la Maria José, al Ferran (sempre en contra de tot), a la Yolanda, a la Montse, a la Gemma... perquè sense el seu ajut i el seu recolzament no hagués estat possible fer un nou experiment i un nou laboratori en tan poc temps. A la Mari Carmen, per haver tingut cura de les meves flors cada vegada que he estat fora. També mereix ser agraït el personal dels tallers (el José Carlos encapaçalant la llarga llista) que m'ha ajudat moltíssim a dur a terme uns projectes complicadíssims (algunes coses les han fet una mica a contracor, però sense queixar-se gaire); a la gent amable d'IT que sempre ha tingut temps de respondre les meves preguntes encara que moltes hagin estat tontes.

En segon lloc he de mencionar el meu supervisor, Morgan Michell (també conegut com a Mitchell Morgan), al que a vegades he hagut de donar alguna petita empenta per poder acabar les coses a temps – s'ha anat queixant moderadament però ha acabat sobrevisquent. També, (ho escriure en anglès perquè ho entengui). *I would like to thank Eugene Polzik who made all this possible.* Mario (més català que el pa amb tomàquet), Herbert, Marco, Zehui, Marcin, Florian i Ale han integrat el grup del que he format part i vull donar-los les gràcies per les experiències que m'han regalat i que no seran oblidades ni demà ni passat demà.

Lluis Torner i Dolors Mateu, com a director i gerent de l'ICFO respectivament, foren peces imprescindibles per a dur a terme la meva tesi doctoral i no puc fer altra cosa que mencionar els seus noms com a mostra de gratitud cap a ells i cap a la institució que representen. D'altra banda, tots els investigadors trobats a l'ICFO, les seves vides, els seus estímuls i les seves experiències conformen un bagatge important per a mi: Caitriona, Petru, Ian, Dobryna, Srdjan, Matteo, Carsten, Felix, Marc, Tristán i la resta de comunistes del passadís roig en el seu conjunt romandran ben amunt en aquesta llista.

En relació a la meva família començaré anomenant a la meva àvia que, als seus 82 anys, continua sent la més llesta de tots nosaltres. Assenyalar a la meva mare, que mai no em perdonà no haver-me fet dentista. També al meu pare, que sempre ha respost a cadascuna de les meves tonteries amb la mateixa frase: "doncs si a tu et fa feliç...". A Zlatko el meu "šudili", la meva ànima bessona, per la seva amistat eterna i per recolzar-me en tot malgrat la distància, moltes gràcies.

Vull mencionar a tots els homes que durant aquest període de temps han demanat la meva mà i he hagut de rebutjar perquè la meva mare no els hagués admès per pobres (és una broma, no tinc el costum d'escoltar ningú). També al noi desconegut que des del portal de casa i durant llargues nits m'ha acompanyat amb el seu bongo, el so insistent del qual m'ha habituat a ser capaç de dormir en qualsevol situació i ha fet que allargués les meves hores de treball durant aquest procés d'ensenyament. Vull també que quedin aquí unes paraules relatives al barri barceloní del Raval, en el que he viscut envoltada d'immobles esquerdats, com el meu, i en el que he compartit experiències insòlites amb molts membres del submón que hom pot trobar-hi: el venedor de butà pakistanès que cada dissabte ha tingut la bondat de despertar-me amb els seus crits, al seu company gitano que arriba posteriorment amb la seva música i els seus potents altaveus, a la senyora Maria, que m'ha subministrat formatges i part de la seva ànima a la seva tenda Rosa d'Abril.

Seguidament no puc fer altra cosa que manifestar el meu agraïment a la Generalitat i als ciutadans de Catalunya (també coneguts com a "gent normal"), amb els impostos dels quals la meva tesi ha pogut veure la llum. Queda aquí per escrit el meu compromís de romandre sempre com a ambaixadora fidel d'aquest poble, vagi on vagi, elogiant les seves virtuts i perdonant el seus pecats.

Per finalitzar, i d'entre tot el que m'enduc d'aquest país, també apuntar l'existència d'un ésser per a mi molt especial, en Markus, que m'ha ajudat moltíssim, aguantant el que no està escrit.

Introduction

Background

A squeezed state is a special quantum mechanical state characterised by minimum noise below the standard quantum limit. In particular, the noise properties are modified so that e.g. amplitude or phase have an uncertainty below the standard quantum limit (for the amplitude noise this leads to noise below shot-noise limit).

The first experimental realisation of squeezing was obtained at Bell labs by four wave mixing in a sodium vapour [64]. They achieved almost 1 dB of noise reduction below standard quantum limit. An alternative technique for squeezed light generation is the phase-sensitive amplification in an optical-parametric oscillator (OPO). The first experimental realisation of squeezing in an OPO was performed in 1986 [74] resulting in almost 3 dB of noise reduction. In 1987 parametric downconversion was used to generate pulsed squeezed light [63]. It resulted in squeezed pulses of 100 ps length 0.6 dB below shot-noise level. In 1992 the record level of quadrature noise suppression in an OPO was pushed to 6 dB below the standard quantum limit [53]. This result was improved in 1998 to 6.2 dB [58]. In recent years this technique has benefited from advances in nonlinear materials, low-loss coatings, and low-noise detectors. This resulted in dramatic improvements in degree of squeezing close to 10 dB below standard quantum limit [66, 70].

The underlying mechanism which results in quadrature squeezing was investigated theoretically in a number of publications. Walls and Millburn were the first to estimate the achievable amount of squeezing in an OPO [45]. They predicted perfect squeezing to be found at the threshold of the optical parametric oscillator. However, the experimental results showed that the best squeezing is seen at pump power being equal to half the threshold [6]. Caves investigated the quantum properties of noise of the linear amplifier [14], and introduced the idea of using squeezed light in the context of improving the sensitivity of gravitational wave detectors [13]. Caves and Schumaker investigated two-mode squeezed states [60] thus extending the previous single mode squeezing to a more general case. Yurke wrote about the use of cavities in the squeezed state generation [77], suggesting that the use of the cavity around the nonlinear material would enhance the downconversion into the mode of the cavity and therefore increase the amount of generated squeezing. Collet and Gardiner introduced a very intuitive approach for understanding the mechanics of squeezing via input-output relations of the cavity [16]. Throughout this thesis we will use the method and notation introduced by Collet and Gardiner.

Squeezed light is not only a special quantum mechanical state but has also several applications: Any measurement that uses only one quadrature for detection can be improved to a sensitivity below the standard quantum limit by using squeezed light for the measurement. Following the proposal by Caves [13] squeezed light was used to improve interferometric measurements. To our knowledge the first experiment which employed squeezed light to improve a measurement sensitivity was made at University of Texas in 1987 [75]. In that experiment the squeezed light was used to improve the detection of phase modulation in an interferometer. The measurement resulted in 3 dB increase in signal to noise ratio. In the same year an increase in sensitivity below the vacuum limit was demonstrated in polarisation interferometry [23]. Here signal to noise ratio was improved by 2 dB. Squeezed light was also used to improve the results of spectroscopic measurements [53]. They have improved the sensitivity for detection of Doppler-free resonances in saturation spectroscopy of atomic cesium. The observed sensitivity enhancement was more than 3 dB.

The improvement of the sensitivity of the interferometers can be used in practice for the detection of gravitational waves. At the moment the most sensitive classical gravitational wave detector is LIGO (Laser Interferometer Gravitational wave Observatory) with the interferometer arm length of 2 to 4 km. A strong gravitational wave would change the arm lenght by at most 10^{-17} m. The high sensitivity necessary for this measurement can currently only be reached at low frequencies (below 1 kHz). At high frequencies the detection is limited by the standard quantum limit. Here the measurements below standard quantum limit could be performed using squeezed light. This application was the motivation to be built a source of squeezed light with very high level of squeezing close to 10 dB below shot-noise level [70].

In addition, the squeezed light is proposed as an important component for light atom interaction for quantum memories. For example squeezed light can be stored and retrieved in quantum memories [33]. Since the squeezed light needs to coupled to the atoms forming the quantum memory the squeezed light needs to be resonant to the respective atomic transition. As the atom will only absorbe the resonant part of the light a narrowband tunable squeezing source is required. Controlled storage and retrieval of light can be achieved in a EIT (Electromagnetically-Induced Transparency) scheme. Here a dressing laser in a λ-type atomic level scheme generates a transparency window for light on the second atomic transition. Switching of the dressing laser can store and retrieve the light inside the medium. Also here the squeezed light needs to be narrowband in order to fit into the transparency window, but also pulsed to spatially fit into the ensemble of atoms. Recently, the delay of the squeezed light in the EIT medium was also shown experimentally. In [2] the storage of 600 ns pulse in a rubidium vapor cell for 1 μs was demonstrated using electromagnetically induced transparency. While the input light squeezing was 1.86 dB the recovered squeezing was reduced to 0.21 dB. Similarly, in [30] the experimental delay of squeezed light was shown using EIT, but also for entangled squeezed light beams. They started with the input squeezing of 3.2$\pm$0.5 dB and recovered 2.0$\pm$0.5 dB of squeezing at the EIT output. For the storage and retrieval of entangled squeezed light they observed a 2.2 μs delay. In [31] was experimentally shown the storage and retrieval of the squeezed state using EIT in a sample of cold rubidium-87 atoms. The squeezed vacuum pulse had a temporal width of 930 ns and the obtained delay was of 3 μs.

This technology has several future applications in the context of quantum information. On this subject exist several theoretical proposals of which many are expected in near future to achieve the experimental realisation . Using entangled states of squeezed light for storage allows for the realisation of quantum repeaters in order to increase the distance of entanglement [17]. On the other hand, pulsed squeezed states can also be used to improve the fidelity of the quantum teleportation of information between atoms and light [62, 32]. Also squeezed light can be used for improving spin squeezing in atomic systems [39].

For many of the above mentioned applications it is important to develop sources of squeezed light resonant to atomic transitions. Cesium resonant squeezed light was demonstrated in a number of experiments [53, 59]. Fast development of the cesium resonant sources of nonclassical light was possible due to the wavelength of cesium D2 at 852 nm where KNbO crystals were readily available. New technology development enabled the demonstration of squeezing at the rubidium resonance [1, 2, 34, 67]. These experiments use distinct methods: squeezing in a waveguide [1] and downconversion in an OPO [2, 34, 67]. In the latter case, squeezing at the rubidium D1 line was achieved in a subthreshold OPO using a Ti:Sapphire laser as pump and periodically poled potassium titanyl oxide phosphate (PPKTP) as nonlinear medium [67, 34, 2]. The noise suppression of this method was shown to be more than 5 dB [34].

This Thesis

This thesis presents an experimental and theoretical investigation of the effect of the pump laser's phase noise on the generation of quadrature squeezed light in an optical parametric oscillator. The experimental objective of this thesis project was the production of squeezed light resonant to the rubidium D1 transition. We employ for this purpose the phase-sensitive amplification in a subthreshold optical parametric oscillator (OPO), a proven technique for the generation of squeezing [53]. Such non-classical light is required for many quantum information tasks based on quantum memories of light [24]. The theoretical investigation considers the effect of the frequency fluctuations, as e.g. caused by phase noise of the pump laser, on the observable squeezing in the regime of quasi-stationary fluctuations. Our analysis shows that the system can be made immune to random frequency drifts.

Efficient interaction of the squeezed light with the atomic ensembles requires its wavelength to be resonant to the respective atomic transition. At the time when this thesis started and the squeezing source was designed the only available sources of squeezed light resonant to any atomic transition existed for cesium resonance [53]. These sources used a Ti:Sapphire laser as a pump source. Employing diode lasers for the production of squeezed light would allow tunable operation in a variety of wavelength ranges beyond the range accessible with Ti:Sapphire lasers. Thus, many important atomic transitions could be addressed with diode lasers so that diode-laser-based squeezing would significantly extend the range of possible squeezing experiments. However, the phase noise of diode lasers could degrade the squeezing generated by such a system. To our knowledge and at the time this document is written no other optical parametric oscillator based source of squeezed light exists that is pumped with a diode laser and resonant to an atomic transition.

The experimental system built in the course of this thesis consists of a PPKTP-based subthreshold OPO pumped by a frequency-doubled diode laser. Here we show that taking into consideration the effect of frequency fluctuations on the observable squeezing in the regime of the quasi-stationary fluctuations one can make the system immune to random frequency drifts. The experimental squeezing apparatus we use, including laser, doubling system, and stabilisation, use standard techniques and could be applied to a variety of other wavelengths.

The thesis is structured as follows:

In the chapter 1 we describe the development of optical parametric oscillators as a sources of squeezed light for quantum memories. Firstly, we present there general ideas on parametric downconversion. We then derive the theoretical description of the process of downconversion in a subthreshold optical parametric oscillator and the formulas necessary for an estimation of the achievable level of squeezing.

Chapter 2 describes the experimental apparatus. First, we summarize the design of the cavity and the properties of the nonlinear crystal. Second, we specify the diode laser and the doubling cavity system we use, and we describe the implementation of the locking systems used for the laser system and the optical parametric oscillator cavity stabilisations. Third, we discuss the amplification gain and the detection efficiency. Finally, we give a full overview of the experiment and we present the squeezing results.

In chapter 3 we analyse the effects of phase noise on quadrature squeezing and describe a technique to eliminate its effect. First, we discuss the origin of the phase noise for diode laser systems. Second, we derive the observable squeezing taking into account the effects of quasi-static frequency fluctuations. Third, we show how the effects of the phase noise can be eliminated and, last but not least,we compare the theoretical prediction with our experimental results.

Publications and presentations

The work presented in this thesis resulted in the following publication:

A. Predojević, Z. Zhai, J.M. Caballero, and M.W. Mitchell, *Rubidium resonant squeezed light from a diode-pumped optical-parametric oscillator,* Phys. Rev. A 78, 063820 (2008)

The author participated in other experiments not presented in this thesis:

F. Wolfgramm, X. Xing, A. Cerè, A. Predojević, A. M. Steinberg, and M. W. Mitchell, *Bright filter-free source of indistinguishable photon pairs,* Opt. Express 16, 18145-18151 (2008)

A. Cerè, V. Parigi, M. Abad, F. Wolfgramm, A. Predojević, and M. W. Mitchell, *Narrow-band tunable filter based on velocity-selective optical pumping in an atomic vapor,* arXiv:0812.2326v1

The work presented in this thesis was presented at the following meetings

- Quantum and Nonlinear Optics School 2006, Humlebaek, Denmark
- CLEOEurope 2007, Munich, Germany

- International School and Conference on Optics and Optical Materials - ISCOM07 , Belgrade, Serbia
- QIPC 2007 International Conference on Quantum Information Processing and Communication , Barcelona, Spain
- CEWQO 2008 15th Central European Workshop on Quantum Optics 2008 Belgrade, Serbia

Contents

Chapter 1

Quantum theory of the OPO

In this chapter we explain in detail the Optical Parametric Oscillator (OPO). We derive important formulae and establish the notation used throughout this thesis. First, we introduce general ideas on parametric downconversion. Later, we present the quantum theory of squeezing in an OPO and derive the spectrum of the OPO output field.

1.1 General facts on OPO and downconversion

The optical parametric oscillator is an optical resonator containing a nonlinear crystal. The nonlinear interaction process taking part in the OPO is called parametric downconversion. It converts the field with frequency 2ω (in this document called the pump field) into two fields with frequencies ω_- and ω_+. In this process a photon with energy $2\hbar\omega$ is converted to one photon with energy $\hbar\omega_-$ and another one with energy $\hbar\omega_+$ with $\omega_- + \omega_+ = 2\omega$, so that the energy is conserved [46]. The two output fields are called signal and idler out of historical reasons. The pump field (2ω) can be resonant to the cavity, however here we will discuss the OPO with nonresonant (single pass) pump. The downconversion process occurs even when the crystal is not placed inside a cavity. Having the crystal in the cavity enhances the downconversion into the modes of the cavity. The OPO is said to work in degenerate regime if the signal and idler fields have same energy and polarisation, i.e. they are indistinguishable. By contrast, the OPO is nondegenerate if the signal and idler fields can be distinguished by polarisation and/or frequency. Concerning the polarisation, the signal and idler fields either share the same polarisation (type I downconversion) or have perpendicular polarisation (type II downconversion). We will describe here a type I OPO operated in degenerate regime. One can understand the process of downconversion in an OPO as the inverse process of the cavity enhanced second harmonic generation (SHG) [46]. Nevertheless, there is an important difference between these two processes: SHG will give a coherent output for any nonzero pump power. By contrast, an OPO (unless it is seeded) will not give a coherent output until the pump power reaches certain value. This power limit is called the threshold of the OPO. While the common interest in OPO's lies in output above threshold where OPO's are used as coherent sources of light over a wide spectral range, we will investigate the sub-threshold OPO.

The OPO below threshold shows interesting quantum mechanical characteristics. Behaving as a phase sensitive amplifier [61] it can amplify/deamplify the quadrature noise of a coherent input field. In the absence of coherent input light the OPO modifies the quadrature noise of the vacuum fluctuations. Apart from the manipulation of the vacuum and coherent state noise levels the subthreshold OPO can be used for production of non-degenerate quadrature entangled states and single-photon states.

1.2 Squeezed state

Generally speaking a squeezed state is a modified coherent state in which the distribution of canonical variables over the phase space has been altered in such a way that the variance of one variable is reduced at the cost of an increase in the variance of the other variable, see e.g. [6, 61, 44]. The two canonical variables under investigation in this thesis are the two quadratures of the electromagnetic field.

Here, we define the form which the phase quadrature operator has throughout this thesis

$$q_\theta = \frac{1}{\sqrt{2}}(ae^{-i\theta} + a^\dagger e^{i\theta}) \tag{1.1}$$

where a, $a^\dagger$ are photon annihilation and creation operators fulfilling the commutation relation $\left[a, a^\dagger\right] = 1$ and θ is the phase. This operator behaves as the canonical conjugate of the phase quadrature operator with the phase shifted by $\pi/2$. The commutator value is the following

$$\left[q_\theta, q_{\theta+\pi/2}\right] = i. \tag{1.2}$$

Therefore one can deduce the respective Heisenberg uncertainty relation

$$\langle q_\theta, q_\theta \rangle^{1/2} \left\langle q_{\theta+\pi/2}, q_{\theta+\pi/2} \right\rangle^{1/2} \geq \frac{1}{2} \tag{1.3}$$

independent of the quantum state. Here $\langle q_\theta, q_\theta \rangle$ is the variance of the operator q_θ. The definition of the variance (and covariance) is given in the appendix A.2. For coherent and vacuum states the quadrature variance is independent of the phase θ and always equal to $1/2$. Consequently, they are states of minimum uncertainty with respect to equation 1.3 . On the other hand, the above given definition of a squeezed state yields the property

$$\langle q_\theta, q_\theta \rangle < \frac{1}{2} \tag{1.4}$$

for the quadrature measured at the phase θ, i.e. a state for which the variance for one quadrature is smaller than for a coherent state. The phase diagram comparing quadrature of vacuum and squeezed state is showed in Figure 1.1.

Using the definition for the normally ordered variance[1]

[1] Here the $\langle :: \rangle$ notation is used for normal ordering of the operators. For normal ordering the operators are expanded with respect to creation and annihilation operators of the photons and sorted so that all creation operators are left of all the annihilation operations. During sorting the respective commutation relations are neglected.

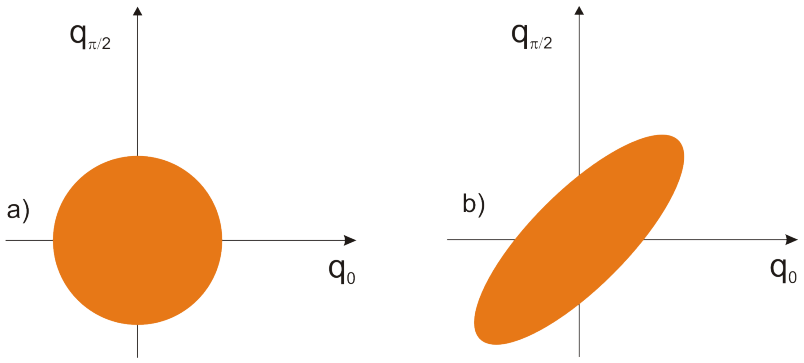

Figure 1.1: Phase-space diagram comparing a) vacuum state and b) squeezed vacuum state. The area coloured in orange represents the region of uncertainty defined by the equation 1.3.

$$\langle : q_\theta, q_\theta : \rangle = \langle q_\theta, q_\theta \rangle - 1/2 \tag{1.5}$$

the definition of the squeezed state can be simplified to

$$\langle : q_\theta, q_\theta : \rangle < 0. \tag{1.6}$$

1.3 Quantum Theory of the OPO

The theory work on squeezing in an OPO dates (as explained in introduction) from the beginning of 80's. This ample work includes several methods to approach the problem of squeezing in a parametric oscillator. Among many important publications on this subject we need to point out the importance of the work by Caves [13, 14, 15, 60], by Walls and Millburn [45], and by Yurke [77].

Nevertheless, we have decided to follow throughout this thesis the approach given by Collett and Gardiner [16]. We choose this approach because it is very intuitive. We also base all the further calculations presented in this thesis on modification of this calculation.

Collett and Gardiner derive the Bogoliubov transformation (to establish the relation) between the output field of the OPO with the vacuum mode entering the cavity. The general form of the Bogoliubov transformation is the following:

$$\begin{aligned} b &= \mu a + \upsilon a^\dagger \\ b^\dagger &= \mu^* a^\dagger + \upsilon^* a \end{aligned} \tag{1.7}$$

where a, $a^\dagger$ and b, $b^\dagger$ are (bosonic) creation and annihilation operators fulfilling the $\left[a, a^\dagger\right] = 1$, $\left[b, b^\dagger\right] = 1$ commutation relations, respectively. The Bogoliubov transformation is a canonical transformation of these operators. Due to the commutation relations the prefactors have to obey the relation

$$|\mu|^2 - |\upsilon|^2 = 1. \tag{1.8}$$

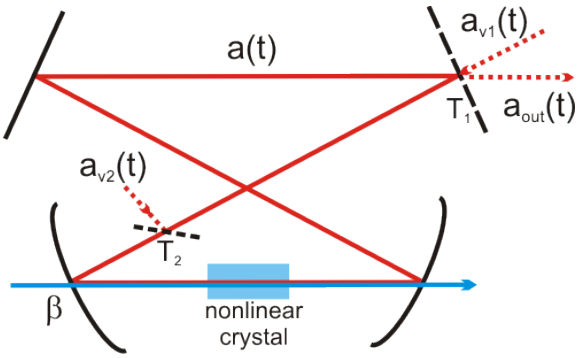

Figure 1.2: The OPO cavity. The vacuum field can enter through the output coupler. The intracavity losses also bring in the vacuum field which in the equations can be modeled as a leaky mirror or a beamsplitter. The a(t) represents the field inside the cavity. The nonlinear crystal is pumped by the constant classical pump field β.

Following the treatment of Collett and Gardiner we start the calculation from the quantum Langevin equation of the OPO cavity

$$\dot{a} = -\frac{i}{\hbar}[a, H_{sys}] - (k_1 + k_2)\, a + \sqrt{2k_1}a_{v1} + \sqrt{2k_2}a_{v2} \tag{1.9}$$

where a and $a^\dagger$ denote annihilation and creation operators of the cavity mode with frequency ω_0, k_1 and k_2 denote the loss rates through the output coupler and due to intracavity losses, and a_{v1} and a_{v2} denote the annihilation operators of the (vacuum) field entering the cavity due to output coupler and intracavity losses.

The field decay rate due to the output coupler transmission can be written as

$$k_1 = \frac{T_1}{2\tau} \tag{1.10}$$

where T_1 is the transmission of the output coupler, and τ=$(FSR)^{-1}$. Here FSR is the free spectral range of the OPO cavity. We will treat the intracavity losses as a vacuum leak through a mirror (Fig.1.2)

$$k_2 = \frac{T_2}{2\tau} \tag{1.11}$$

where T_2 are the intracavity losses. The experimental characterisation of the intracavity losses in our experiment is described in section 2.1.4. The cavity losses for a slowly decaying cavity are treated in detail in [6, 56].

The Hamiltonian describing the parametric conversion is given as [22]

$$H_{sys} = \hbar\omega_0 a^\dagger a + \frac{i\hbar}{2}\left(\varepsilon e^{-i\omega_p t}\left(a^\dagger\right)^2 - \varepsilon^* e^{i\omega_p t}a^2\right). \tag{1.12}$$

The first term describes the energy of photons inside the cavity while the second term models the nonlinear interaction induced by the pump field with frequency ω_p. Here $\varepsilon = g\beta$ is the nonlinear coupling, β is the pump field and g is a

coupling constant which is real and proportional to the crystal nonlinearity. The phase ϕ of the nonlinear coupling is determined by the phase of the pump field $\varepsilon = g\left|\beta\right| e^{i\phi}$. The nonlinier coupling is responsable for the parametric gain of the oscillator. The classical description of the parametric gainis given in the appendices B.2 and B.3.

After inserting the Hamiltonian (equation 1.12) the equation 1.9 gets the following form

$$\dot{a} = -i\omega_0 a + \varepsilon e^{-i\omega_p t} a^\dagger - (k_1 + k_2)\, a + \sqrt{2k_1} a_{v1} + \sqrt{2k_2} a_{v2}. \tag{1.13}$$

In the next step the equation 1.13 is transformed to rotating reference frame by applying, $a = \tilde{a} e^{-i\omega_0 t}$. It is equivalent to a transformation to the interaction picture by shifting the zero of the energy scale to the value of $\hbar\omega_0$. This yields

$$\dot{\tilde{a}} = \varepsilon e^{-i(\omega_p - 2\omega_0)t} \tilde{a}^\dagger - (k_1 + k_2)\, \tilde{a} + \sqrt{2k_1} \tilde{a}_{v1} + \sqrt{2k_2} \tilde{a}_{v2}. \tag{1.14}$$

Then the Fourier transform $(2\pi)^{-\frac{1}{2}} \int dt e^{i\omega t} \tilde{a}(t) = \tilde{a}(\omega)$ (explained in more detail in section A.1) is applied on both sides of the equation. For $\omega_p = 2\omega_0$, the final forms of the equation 1.13 and its Hermitian conjugate are

$$\begin{aligned} -i\omega\tilde{a}(\omega) &= \varepsilon\tilde{a}^\dagger(-\omega) - (k_1 + k_2)\,\tilde{a}(\omega) + \sqrt{2k_1}\tilde{a}_{v1}(\omega) + \sqrt{2k_2}\tilde{a}_{v2}(\omega) \\ i\omega\tilde{a}^\dagger(\omega) &= \varepsilon^*\tilde{a}(-\omega) - (k_1 + k_2)\,\tilde{a}^\dagger(\omega) + \sqrt{2k_1}\tilde{a}^\dagger_{v1}(\omega) + \sqrt{2k_2}\tilde{a}^\dagger_{v2}(\omega). \end{aligned} \tag{1.15}$$

Here, it is important to point out that the Fourier transform is performed considering ε to be a constant in time. This approach is justified in the case of monochromatic pump laser filed with large amplitude so that it does not need to be treated quantum mechanically.

From the equations 1.15 one can find the expression for the field circulating in the cavity $\tilde{a}(\omega)$

$$\begin{aligned} \tilde{a}(\omega) &= (-i\omega + (k_1 + k_2))\left(\sqrt{2k_1}\tilde{a}_{v1}(\omega) + \sqrt{2k_2}\tilde{a}_{v2}(\omega)\right) B^{-1} \\ &\quad + \varepsilon\left(\sqrt{2k_1}\tilde{a}^\dagger_{v1}(-\omega) + \sqrt{2k_2}\tilde{a}^\dagger_{v2}(-\omega)\right) B^{-1} \end{aligned} \tag{1.16}$$

where B is

$$B = \left[(k_1 + k_2) - i\omega\right]^2 - \left|\varepsilon\right|^2. \tag{1.17}$$

This field is related to the field leaving the cavity by the boundary condition [16] (input-output relation)[2]

$$\sqrt{2k_1}\tilde{a}(\omega) = \tilde{a}_{v1}(\omega) + \tilde{a}_{out}(\omega). \tag{1.18}$$

This allows one to derive the Bogoliubov transformation from input to output fields:

$$\tilde{a}_{out}(\omega) = C_1\tilde{a}^\dagger_{v1}(-\omega) + C_2\tilde{a}^\dagger_{v2}(-\omega) + C_3\tilde{a}_{v1}(\omega) + C_4\tilde{a}_{v2}(\omega) \tag{1.19}$$

[2]It is important to note that the equation 1.18 is a result of approximation $T_1 \ll 1$ and is valid only under this condition.

with

$$\begin{aligned} C_1 &= 2\varepsilon k_1 B^{-1} && (1.20)\\ C_2 &= 2\varepsilon\sqrt{k_1 k_2} B^{-1} && (1.21)\\ C_3 &= \left[k_1^2 - (k_2 - i\omega)^2 + |\varepsilon|^2\right] B^{-1} && (1.22)\\ C_4 &= 2\sqrt{k_1 k_2}\left((k_1 + k_2) - i\omega\right) B^{-1}. && (1.23) \end{aligned}$$

From here on all frequencies and rates are scaled to the cavity linewidth $\delta\nu = k_1 + k_2$. The new parameters used are: $\Omega = \omega\left(k_1 + k_2\right)^{-1}$, $\eta = k_1\left(k_1 + k_2\right)^{-1}$, $1 - \eta = k_2\left(k_1 + k_2\right)^{-1}$, $\mu = \varepsilon\left(k_1 + k_2\right)^{-1}$. Parameters η and μ can be directly determined experimentally. The parameter η is the so called cavity escape efficiency. In practice, it is the ratio between the transmission of the output coupler and the sum of both the intracavity losses and the transmission of the output coupler $\eta = T_1\left(T_1 + T_2\right)^{-1}$. Parameter μ represents the ratio of the pump field used in the experiment and the pump field necessary for reaching the threshold. Consequently, μ is equal to the square root of the ratio of pump power to threshold power $\mu = \sqrt{P_{pump} P_{th}^{-1}}$.

The output field expressed with these scaled parameters is

$$\begin{aligned} \tilde{a}_{out}(\omega) &= f_1 \tilde{a}_{v1}(\omega) + f_2 \tilde{a}_{v1}^{\dagger}(-\omega)\\ &+ f_3 \tilde{a}_{v2}(\omega) + f_4 \tilde{a}_{v2}^{\dagger}(-\omega) && (1.24) \end{aligned}$$

with

$$\begin{aligned} f_1 &= \left(\eta^2 - (1 - \eta - i\Omega)^2 + |\mu|^2\right) A^{-1} && (1.25)\\ f_2 &= 2\eta\mu A^{-1} && (1.26)\\ f_3 &= 2\sqrt{\eta(1-\eta)}\left(1 - i\Omega\right) A^{-1} && (1.27)\\ f_4 &= 2\mu A^{-1}\sqrt{\eta(1-\eta)} && (1.28)\\ A &= (1 - i\Omega)^2 - |\mu|^2. && (1.29) \end{aligned}$$

The noise in the output field of the OPO is usually characterised using a homodyne detection geometry [61, 73] where our output field $\tilde{a}_{out}(\omega)$ is mixed with the strong coherent beam called local oscillator (LO). The mixing of the two fields is followed by balanced detection [6] where the light beam consisting of the two above mentioned fields is split in two and sent onto two detectors. The currents produced by these two detectors are electronically subtracted and the obtained signal is fed into a spectrum analyser to measure the noise spectrum. In the following we will deduce the signal we measure with the spectrum analyser.

The output current after subtraction of the two photodetector signals is proportional to the difference in photon counting rate [61]

$$\Delta I_{det} \propto \langle n_{D1}(t)\rangle - \langle n_{D2}(t)\rangle \propto \beta_{LO}\langle q_\theta(t)\rangle = \frac{\beta_{LO}}{\sqrt{2}}\left\langle \tilde{a}_{out} e^{-i\theta} + \tilde{a}_{out}^{\dagger} e^{i\theta}\right\rangle. \quad (1.30)$$

The n_{D1} and n_{D2} are the photon counting rates at the two detectors. Note that the signal is proportional to the amplitude of the local oscillator β_{LO} so that the signal aplitude can be adjusted. In the following we are not anymore interested in the precise amplitude of the signal, but only in its relation to quantum noise. Therefore we will neglect this constant proportionality factor. Here we leave out the proportionality factor since later on we will be only interested in the deviation from the mean value compared to the mean value.

The power spectral density of this signal is measured by the spectrum analyser. Due to the Khinchin–Kolmogorov (also known as Wiener–Khinchin) theorem this spectral density is equal to the Fourier transform of the respective autocorrelation signal, i.e.

$$\frac{1}{2}S(\omega) = \frac{1}{\sqrt{2\pi}} \int \left\langle q_\theta^\dagger(t), q_\theta(t+\tau) \right\rangle e^{i\omega\tau} d\tau. \tag{1.31}$$

This equation defines the squeezing spectrum $S(\omega)$ (with the factor $1/2$ due to normalisation). It is directly measured by the spectrum analyser (up to the above proportionality factor squared). Note that the squeezing spectrum $S(\omega)$ for the vacuum state is equal to one. Therefore by blocking the signal input of the homodyne detection it is possible to directly measure the proportionality factor between the measurement with the spectrum analyser and the squeezing spectrum as defined above. Dividing the signal with the squeezed input by the signal with vacuum input only, it is possible to directly measure the squeezing spectrum $S(\omega)$. Note that in equation 1.31 we use the (temporal) covariance instead of the autocorrelation function, since we are only interested in the deviation of the autocorrelation function from its mean value, while the mean value will only give a contribution to $S(\omega)$ at value $\omega = 0$ where we do not measure. If we assume that $q_\theta(t)$) is a randomly fluctuating observable where the average value does not change with time, i.e. it is a stationary random process, then for the correlation of $q_\theta(t)$) in frequency space the relation 1.31 is equivalent to [44]

$$\left\langle \tilde{q}_\theta^\dagger(\omega), \tilde{q}_\theta(\omega') \right\rangle = \frac{1}{2\pi} \iint \left\langle q_\theta^\dagger(t), \tilde{q}_\theta(t') \right\rangle e^{-i\omega t} e^{i\omega' t'} \, dt \, dt' \tag{1.32}$$

with $t' = t + \tau$ we derive

$$\begin{aligned} \left\langle \tilde{q}_\theta^\dagger(\omega), \tilde{q}_\theta(\omega') \right\rangle &= \frac{1}{\sqrt{2\pi}} \int dt \, e^{i(\omega'-\omega)t} \frac{1}{\sqrt{2\pi}} \int \left\langle q_\theta^\dagger(t), \tilde{q}_\theta(t+\tau) \right\rangle e^{i\omega'\tau} d\tau \\ &= \frac{1}{\sqrt{2\pi}} \int dt \, e^{i(\omega'-\omega)t} \, S(\omega') \\ &= \delta(\omega - \omega') \, S(\omega). \end{aligned} \tag{1.33}$$

with the Fourier transform of $q_\theta(t)$) being

$$\tilde{q}_\theta(\omega) = \frac{1}{\sqrt{2}} \left(\tilde{a}(\omega) e^{-i\theta} + \tilde{a}^\dagger(-\omega) e^{i\theta} \right) = F\left[q_\theta(t) \right]. \tag{1.34}$$

We now want to introduce the normally ordered covariance (the generalization of the equation 1.5) using

$$\left\langle \tilde{q}_\theta^\dagger(\omega), \tilde{q}_\theta(\omega') \right\rangle = \left\langle : \tilde{q}_\theta^\dagger(\omega), \tilde{q}_\theta(\omega') : \right\rangle + \frac{1}{2}\delta(\omega - \omega') \tag{1.35}$$

so that equation 1.33 is converted to

$$\left\langle :\tilde{q}_{\theta}^{\dagger}\left(\omega\right),\tilde{q}_{\theta}\left(\omega'\right):\right\rangle =\frac{1}{2}\left(S\left(\omega\right)-1\right)\delta\left(\omega-\omega'\right). \tag{1.36}$$

Taking into account the non-perfect detection efficiency ($\tilde{q}_{\theta}\left(\omega\right)\rightarrow\sqrt{\eta_{det}}\tilde{q}_{\theta}\left(\omega\right)$) the equation 1.36 is modified to

$$\eta_{det}\left\langle :\tilde{q}_{\theta}^{\dagger}\left(\omega\right),\tilde{q}_{\theta}\left(\omega'\right):\right\rangle =\frac{1}{2}\left(S\left(\omega\right)-1\right)\delta\left(\omega-\omega'\right). \tag{1.37}$$

This equation relates the measured squeezing spectrum $S\left(\omega\right)$ with the normally ordered covariance of $q_{\theta}\left(\omega\right)$.

Using the definition of $q_{\theta}\left(\omega\right)$(equation 1.34) the normally ordered covariance is

$$\begin{aligned}\left\langle :\tilde{q}_{\theta}^{\dagger}\left(\omega\right),\tilde{q}_{\theta}\left(\omega'\right):\right\rangle &= \frac{1}{2}\left\langle \tilde{a}_{out}^{\dagger}\left(-\omega'\right),\tilde{a}_{out}\left(-\omega\right)\right\rangle +\frac{1}{2}\left\langle \tilde{a}_{out}^{\dagger}\left(\omega\right),\tilde{a}_{out}\left(\omega'\right)\right\rangle \\ &+ \frac{1}{2}\left\langle \tilde{a}_{out}\left(-\omega\right),\tilde{a}_{out}\left(\omega'\right)\right\rangle e^{-2i\theta} \\ &+ \frac{1}{2}\left\langle \tilde{a}_{out}^{\dagger}\left(\omega\right),\tilde{a}_{out}^{\dagger}\left(-\omega'\right)\right\rangle e^{2i\theta}.\end{aligned} \tag{1.38}$$

We note that all the terms in the previous equation have contributions of correlations between $+\omega$ and $-\omega$ terms. Due to this we conclude that the reduction of noise in the signal (the squeezing) comes as a consequence of the(anti-)correlations between the sidebands ω and -ω of the output light. If the cavity input states are coherent states or as in our case vacuum states their normally ordered variance is equal to zero (see appendix A.2). This leaves the anti-normally ordered terms of $\tilde{a}_{v1}$ and $\tilde{a}_{v2}$ as only contribution to the normally ordered variance of the output field

$$\left\langle \tilde{a}_{out}^{\dagger}\left(-\omega'\right),\tilde{a}_{out}\left(-\omega\right)\right\rangle =\left\langle \tilde{a}_{out}^{\dagger}\left(\omega\right),\tilde{a}_{out}\left(\omega'\right)\right\rangle =0 \tag{1.39}$$

$$\left\langle \tilde{a}_{out}^{\dagger}\left(\omega\right),\tilde{a}_{out}\left(\omega'\right)\right\rangle =\left(\left|f_{2}\right|^{2}+\left|f_{4}\right|^{2}\right)\delta\left(\omega-\omega^{'}\right) \tag{1.40}$$

$$\left\langle \tilde{a}_{out}\left(-\omega\right),\tilde{a}_{out}\left(\omega'\right)\right\rangle =\left(\left\langle \tilde{a}_{out}^{\dagger}\left(\omega\right),\tilde{a}_{out}^{\dagger}\left(-\omega'\right)\right\rangle \right)^{*} \tag{1.41}$$

$$\begin{aligned}\left\langle \tilde{a}_{out}^{\dagger}\left(\omega\right),\tilde{a}_{out}^{\dagger}\left(-\omega'\right)\right\rangle &= f_{1}^{*}\left(\omega\right)f_{2}^{*}\left(-\omega^{'}\right)\delta\left(\omega-\omega^{'}\right) \\ &+f_{3}^{*}\left(\omega\right)f_{4}^{*}\left(-\omega^{'}\right)\delta\left(\omega-\omega^{'}\right).\end{aligned} \tag{1.42}$$

Using the equations 1.39 - 1.42 we get the squeezing spectrum

$$\begin{aligned}\frac{1}{2}\left(S\left(\omega\right)-1\right)\delta\left(\omega-\omega'\right) &= \frac{1}{2}\eta_{det}\left\{ \left(f_{1}^{*}\left(\omega\right)f_{2}^{*}\left(-\omega\right)^{'}+f_{3}^{*}\left(\omega\right)f_{4}^{*}\left(-\omega^{'}\right)\right)\right. \\ &+ \left.2\left(\left|f_{2}\right|^{2}+\left|f_{4}\right|^{2}\right)\right\} \delta\left(\omega-\omega^{'}\right).\end{aligned} \tag{1.43}$$

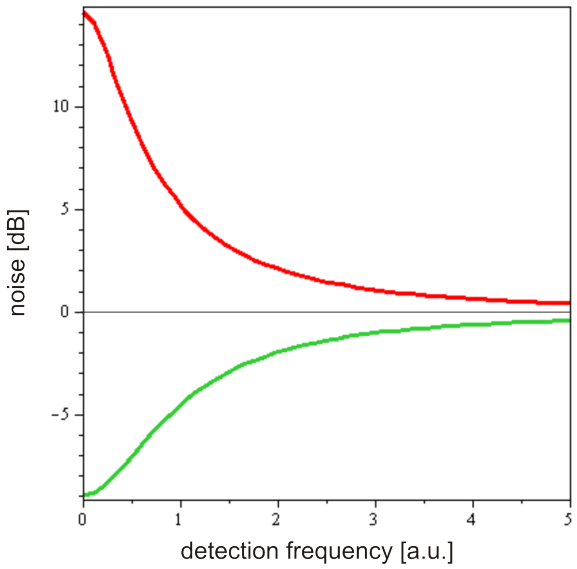

Figure 1.3: The theoretical spectrum of squeezing plotted for the pump power equal to half the threshold. The cavity escape efficiency is assumed to be 90%. The red and green curves represent the antisqueezing and the squeezing values, respectively. The phase in between squeezing and antisqueezing is $\pi/2$.

Obviously the δ- distributions appear on the both sides of equation and can be left out.

Rewriting the equation 1.43 we thus obtain the following result for the squeezing spectrum

$$S(\Omega) = 1 + 4\eta\,|\mu|\,\eta_{det}\left(2\,|\mu| + \left(1 + \Omega^2 + |\mu|^2\right)\cos\left(2\theta - \phi\right)\right)|A|^{-2}\,. \qquad (1.44)$$

The squeezing spectrum $S(\Omega)$ was first shown by [50] and in detail explained in [44].

The squeezing spectrum $S(\Omega)$depends on the relative phase between the phase of the pump field ϕ and the detection phase 2θ. Maximum squeezing is obtained for $2\theta = \phi + \pi$ which yields

$$S(\Omega) = 1 - \frac{4\eta\,|\mu|\,\eta_{det}}{\left(1 + |\mu|\right)^2 + \Omega^2} \qquad (1.45)$$

while maximum antisqueezing is observed for $2\theta = \phi$ with

$$S(\Omega) = 1 + \frac{4\eta\,|\mu|\,\eta_{det}}{\left(1 - |\mu|\right)^2 + \Omega^2}. \qquad (1.46)$$

These two extremes are plotted in figure 1.3 for perfect detection efficiency $\eta_{det} = 1$, escape efficiency $\eta = 0.9$ and pump parameter $\mu = \sqrt{1/2}$.

Chapter 2

Production of Squeezed light

The previous chapter describes the theory of the OPO as a source of a nonclassical light. In this chapter we describe the important elements of the experimental set-up. First, in section 2.1 we analyse the design criteria of the cavity. This includes the choice of non-linear material, and optized focusing into the crystal in order to achieve high conversion efficiency and at the same time avoid thermal lensing. Furthermore, losses e.g. induced by gray-tracking are disscussed in this section. Second, in section 2.2 we specify the details of the laser system. Here, the special locking system is explained which employs a PID controller synthesized on a field-programmable gate array (FPGA). Third, in section 2.3 we discuss the characterisation of the experimental elements to achieve squeezed light. This includes the characterisation of the parametric gain of the OPO and the noise properties of the detector. Finally, we explain the experimental apparatus as a whole and present our squeezing results.

2.1 Construction of the cavity

The OPO described in this thesis uses type I downconversion, and is operated in degenerate regime. It is running subthreshold and is used for production of squeezed vacuum. The cavity is doubly resonant (to signal and idler field which are degenerate) and is designed to provide a narrowband source of rubidium-87 resonant squeezed light.

2.1.1 Modeling of the cavity geometry. Bandwidth

The propagation of the beams in the cavity and the geometry of the cavity can be calculated using the ABCD matrices principle [46]. The Gaussian beams in the cavity are defined by the complex beam parameter q,

$$\frac{1}{q} = \frac{1}{R} - \frac{i\lambda}{\pi w^2} \tag{2.1}$$

where R is the radius of curvature of the beam, λ the wavelength and w the beam spot size.The modes resonant to the cavity reproduce themselves in radius of curvature and beam spot size after one round trip. This statement is valid for any point of the light path in the stable cavity. Consequentially, the q parameter of the beam can be calculated from the following equation:

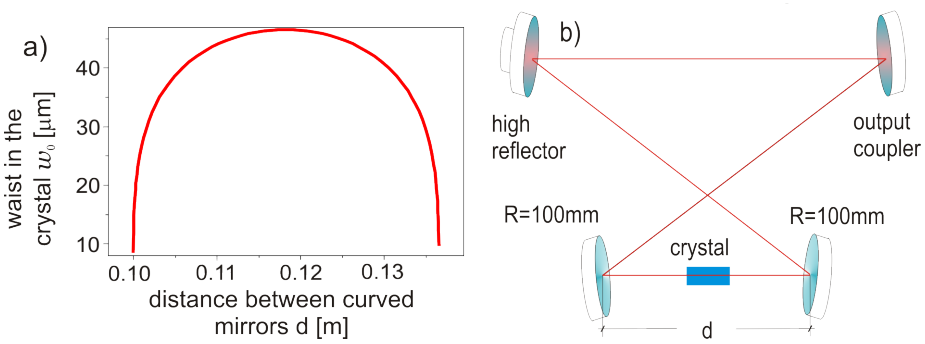

Figure 2.1: a) Waist size w_0 depending on the distance between curved mirrors d. The cavity parameters are: radius of curvature of the mirrors is of 100 mm, cavity lenght $l = 0.6\,m$. The distance d between mirrors of 11,5 cm due to the refractive index of the crystal of n=1.75 yields an optical path of 12,25 cm effectively. b) Schematic of the OPO showing its bow-tie configuration and position of high reflector and the T=7.8% output coupler.

$$q = \frac{A\,q + B}{C\,q + D} \tag{2.2}$$

where A, B, C and D are the components of the ABCD matrix for one round trip in the cavity.

The crystal is placed in the cavity at half distance between the spherical mirrors. This way the light is focused at the center of the crystal. The radius of curvature of the beam at the focus is equal to infinity. This makes it easy to calculate the waist (the spot size at the focus) w_0 knowing the q parameter at the focus

$$w_0 = \sqrt{\frac{\lambda\,q}{\pi}}. \tag{2.3}$$

Optimisation of the waist for maximum conversion efficiency is discussed later in section 2.1.3.

The ABCD matrix for a cavity round trip starting half way between the resonator spherical mirrors can be written in the following way:

$$M = M_{d/2}\,M_R\,M_{l-d}\,M_R\,M_{d/2}. \tag{2.4}$$

The M_R is the ABCD matrix of the spherical mirror with radius of curvature R and $M_{d/2}$, M_{l-d} are the matrices for free space propagation over the length $d/2$ and $l-d$, respectively. Here l is the overall length of the OPO and d is the separation between two spherical mirrors as shown in Figure 2.1b. The ABCD matrices for different optical elements can be found in [46, 56, 38].

To prove the stability of the chosen cavity configuration one can use the stability condition $-1 < \frac{1}{2}(A+D) < 1$ [38] valid for any optical resonator. In the case of our cavity this condition becomes $0 < l - d(l-d)R^{-1} < R$.

Our OPO cavity is a 60 cm long resonator in a bow-tie configuration. The radius of curvature of the spherical mirrors is R=10 cm. The distance between the spherical mirrors is 11.5 cm yielding a beam waist in the crystal of 42 μm.

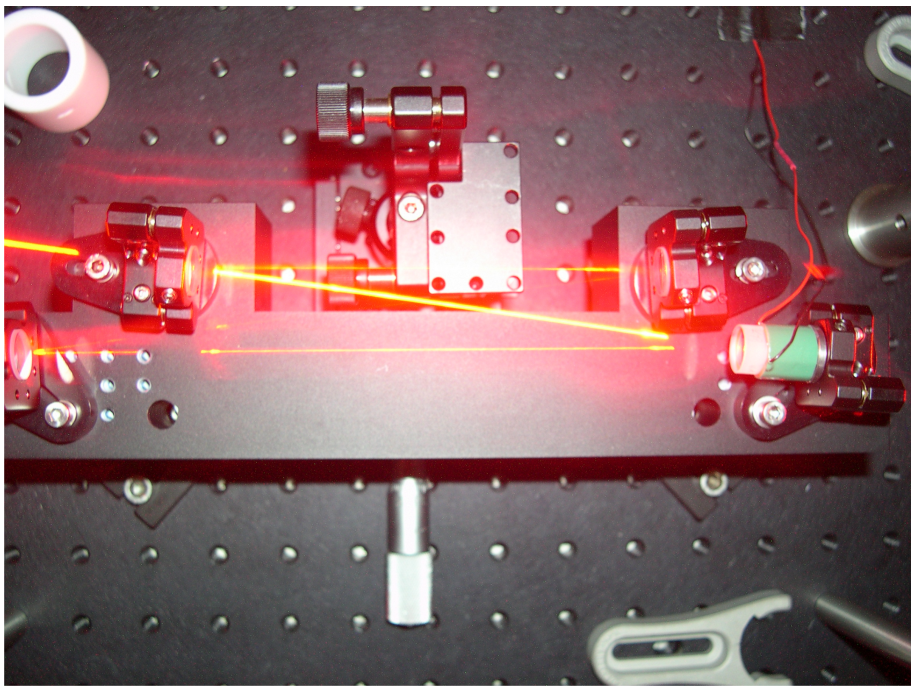

Figure 2.2: The photograph of the empty (i.e.,without crystal) OPO cavity with the alignment beams passing through it.

The dependence of the waist size on the distance between curved mirrors is shown in the figure 2.1a. We chose the waist size taking into consideration both the efficiency of the second harmonic generation and the absorption induced instability. These two points are described in detail in section 2.1.3. The cavity round trip time is equal to $\tau = (l + d)\, c^{-1}$ where c is the speed of light. The free spectral range (FSR) is due to cavity length (60 cm) FSR=τ^{-1}=500 MHz. The measured OPO cavity linewidth is $\delta\nu = 8$ MHz full width half maximum (FWHM). The schematic of the OPO cavity is shown in figure 2.1b. Figure 2.2 is shows the photograph of the OPO cavity.

2.1.2 Nonlinear crystal

To achieve the maximum conversion efficiency the fields interacting in the nonlinear medium should satisfy the phase matching condition $\Delta k = 0$, where k is the wave vector. Completion of this condition guarantees that the phase relation between the interacting fields is maintained along the propagation direction so that the downconverted light in the different regions of the crystal does not interfere destructively. A common way to guarantee the phase matching is to use a birefringent crystal as the nonlinear medium. Proper choice of the birefringent crystal cut can match the refractive indices of the involved fields to fulfill the phase matching condition. Fine tuning of the field phases is usually performed by optimisation of the temperature.

$$\Delta k = k_{2\omega} - 2k_{\omega} = \frac{2\omega}{c}(n_{2\omega}(\omega_{2\omega}, T) - n_{\omega}(\omega_{\omega}, T)). \tag{2.5}$$

Here ω is the frequency of the light, T the temperature and n the refractive index of the crystal.

Unfortunately, birefringent phase matching suffers several disadvantages. If the propagation direction does not coincide with the axis of the crystal the interacting fields suffer spatial walk-off which limits the interaction length of the fields and deteriorates the beam quality. This condition is also known as critical phase matching because of the sensitivity of phase matching to the tilt of the crystal. In addition, for some wavelengths it is not possible to fulfill the phase matching condition.

The light induced polarisation of the nonlinear dielectric material is in second order proportional to the square of the electric field, $P_i^{NL} = \varepsilon_0 \sum d_{ijk} E_j E_k$ [46]. The nonlinearity caused by this second order term of the polarisation is commonly called second order nonlinearity. Nonlinearities of higher order are always present but in our experiment irrelevant. The tensor d_{ijk} is called nonlinear susceptibility tensor. Since E_j and E_k can be permuted without changing P_i the nonlinear susceptibility tensor can be written in the form of a 3×6 matrix:

$$\begin{pmatrix} P_x^{NL} \\ P_y^{NL} \\ P_z^{NL} \end{pmatrix} = \varepsilon_0 \begin{bmatrix} d_{11} & d_{12} & d_{13} & d_{14} & d_{15} & d_{16} \\ d_{21} & d_{22} & d_{23} & d_{24} & d_{25} & d_{26} \\ d_{33} & d_{32} & d_{33} & d_{34} & d_{35} & d_{36} \end{bmatrix} \times \begin{pmatrix} E_x^2 \\ E_y^2 \\ E_z^2 \\ 2E_yE_z \\ 2E_xE_z \\ 2E_xE_y \end{pmatrix}. \tag{2.6}$$

The elements of the d_{ij} characterize the strength of the crystal nonlinearity along a certain direction. It is often the case in birefringent phase matching that the direction of the largest nonlinearity cannot be used as the propagation direction because it does not fulfill the phase matching condition.

In case the phase matching is not fulfilled the fields will suffer phase mismatch of π within the length L_C called the coherence length,

$$L_C = \frac{2\pi}{\Delta k}. \tag{2.7}$$

The problem of phase mismatch and the coherence length is in detail explained in [46].

One can overcome the above mentioned phase matching problems using periodically poled crystals and quasi-phase matching. The technique was suggested in 60's [4, 21], but started to be commercially available a couple of years ago. The quasi-phase matching condition is given by

$$\Delta k = k_{2\omega} - 2k_{\omega} - k_{pp} = \frac{2\omega}{c}(n_{2\omega}(\omega_{2\omega}, T) - n_{\omega}(\omega_{\omega}, T) - k_{pp}(T)) \tag{2.8}$$

where $k_{pp}(T)$ is a poling-induced phase matching correction.

Quasi phase matching is based on spatial modulation of the crystal structure using a DC electric field. The schematic of the poling procedure is shown in Figure 2.1.2.a. In general it is performed on ferroelectric crystals. The modulation

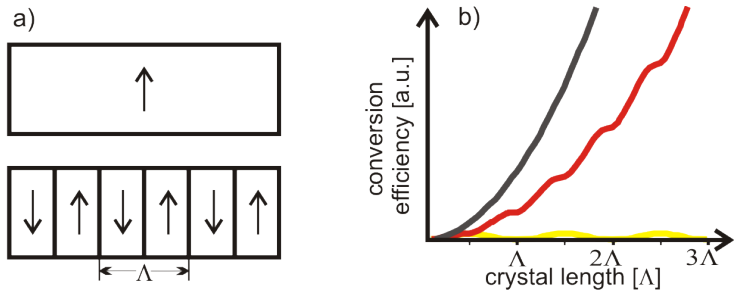

Figure 2.3: a) Schematic of periodic poling: alternating the polarity of a temporarily applied external DC field the bulk crystal forms zones with different crystal orientation favouring in this way correct phase matching b) Power conversion efficiency vs. crystal length for three different cases of mode matching: black - birefringent phase matching; red - quasi phase matching; yellow - no phase matching [3].

of the domains is such that the crystal orientation changes from $+d_{ij}$ to $-d_{ij}$ with periodicity of $2\mathrm{L}_C$. Here d_{ij} is the effective nonlinear coefficient derived from 2.6 for the particular direction of propagation and field polarisation. This way one can synthesise a nonlinear crystal which uses the natural nonlinearity of the material modified to fulfill the phase matching condition. The effective nonlinear coefficient of a periodically poled material will be smaller than d_{ij} and can be calculated as ([3])

$$d(z) = d_{ij}\mathrm{sign}[\cos(\frac{2\pi z}{\Lambda})] = d_{ij}\sum_{m=-\infty}^{m=\infty} G_m e^{ik_m z} \tag{2.9}$$

$$G_m = \frac{2}{m\pi}\sin\left(\frac{m\pi}{2}\right) \tag{2.10}$$

$$k_m = \frac{2\pi m}{\Lambda} \tag{2.11}$$

where Λ is the poling period equal to $2\mathrm{L}_c$, and $k_m = 2\pi m\Lambda^{-1}$ is equal to the correction of the phase matching, k_{pp}, from equation 2.8. The effective nonlinearity $d\,(z)$ shown in equation 2.9 links the effective nonlinear coefficient of the periodically poled material with the nonlinearity for the birefrigent crystal of the same length

$$d_{eff}\,(L) = \frac{2}{\pi}d_{ij}. \tag{2.12}$$

The efficiency of the the birefringent and quasi phase matching are shown in Figure 2.1.2.b.

Frequency conversion processes at low wavelengths suffer from lack of adequate nonlinear materials. Commonly used material for the conversion from IR to UV and vice versa is potassium niobate ($KNbO_3$). For the wavelengths we use phase matching in $KNbO_3$ is not fulfilled and also the transparency range is not wide enough as shown in Table 2.1. Furthermore, with in the limit of

	BBO	$KNbO_3$	KTP	LBO	BIBO	PPKTP
Transparency range [nm]	190-3500	400-4500	350-4500	160-2600	288-2500	350-4500
d_{eff} [pm/V]	2.00	no match	no match	0.74	3.74	9.8

Table 2.1: Comparison of the transparency range and nonlinearity for birefringent and periodically poled crystals commonly used for frequency conversion from UV to IR and vice versa. The nonlinearities d_{eff} for BBO, $KNbO_3$, KTP, LBO BIBO and PPKTP presented here are taken from [18, 51, 71, 55, 26, 42], respectively while the information on transparency ranges for BBO, $KNbO_3$, KTP, BIBO, LBO and PPKTP were taken from [43, 53, 71, 27, 72, 42], respectively. The ranges shown here are not fully applicable to our case since our crystal length is 10 mm and these specifications are made based on measurements on thin crystals (pulsed and ultra-fast applications). The largest nonlinearity showed here and applicable for our wavelengths is the PPKTP nonlinearity of 9.8 pm/V.

its transparency range the use of $KNbO_3$ is limited by the effect called blue light induced infrared absorption (BLIIRA) [53]. Beta barium borate (BBO) is transparent over a larger range than $KNbO_3$ and satisfies the phase matching condition at our wavelength but it has low nonlinearity (Table 2.1). Due to its wide transparency range (Table 2.1), potassium titanyl phosphate (KTP) would be suitable nonlinear material for us. For the last three decades this material has been widely used in different SHG and OPO devices. Unfortunately, the bulk KTP does not fulfill the phase matching condition for 795 nm. Fortunately, KTP exhibits high d_{33}nonlinearity and being a ferroelectric crystal it can undergo the process of poling. The poling procedure on KTP has enabled the frequency conversion at short wavelengths.

The nonlinearity tensor of the bulk KTP is given by

$$d_{ijk}^{KTP}[pm/V] = \begin{vmatrix} 0 & 0 & 0 & 0 & 1.95 & 0 \\ 0 & 0 & 0 & 3.9 & 0 & 0 \\ 1.95 & 3.9 & 15.3 & 0 & 0 & 0 \end{vmatrix}. \tag{2.13}$$

The crystal we used in this experiment was produced by Raicol. It was poled to give phase matching to type I parametric downconversion from 397 nm to 795 nm light. The crystal length is 10 mm and the cross section 1×3 mm. Phase matching was made for light polarized along the crystallographic Z axis. Crystal end faces were antireflection coated for both IR and UV. The poling period was determined using Sellmeier equation [71, 36]

$$n_z^2(\lambda) = 2.3136 + \frac{1.00012}{1 - (\frac{238.31\,nm}{\lambda})^2} - (\frac{\lambda}{7717\,nm})^2 \tag{2.14}$$

where λ is the wavelength of the fundamental beam. The equation 2.14 gives the value of the poling period necessary for our experiment of 3.2 μm. The design of the poling mask determines the optimum working temperature. In Figure 2.4 is shown the dependence of the upconversion efficiency on the temperature. The optimum temperature was found to be close to 25°C. Consequently during the experiment described in this thesis the temperature of the crystal is stablised

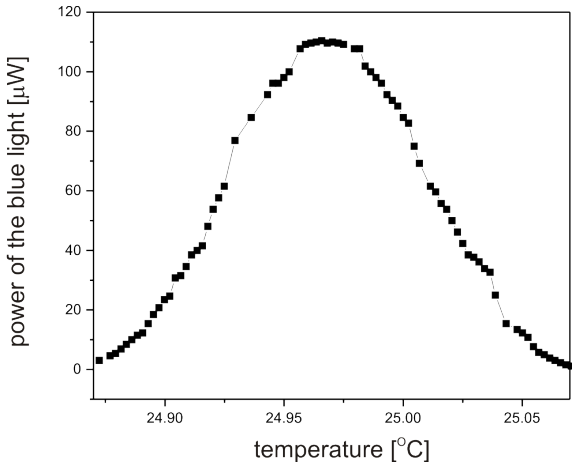

Figure 2.4: Conversion efficiency (the power of the blue light produced) of our PPKTP crystal vs. temperature. This curve was measured using a 5 mW 795 nm beam fed into OPO cavity with cavity mode matching close to 90%. The red light was upconverted to blue 397 mW light. The y-axis shows the power of the produced second harmonic blue light. The temperature was determined based on a four wire measurement on a PT100 sensor. The maximum conversion efficiency was obtained at the temperature close to 25^oC.

to 25^oC using an in-loop temperature control. The temperature control circuit is commercially available from Wavelength Electronics (HTC1500).

2.1.3 Optimal focusing in the crystal and thermal lensing

The SHG efficiency depends linearly on the intensity of the fundamental beam [46]. Unfortunately, excess in power and strong focusing might lead to heating and damage of the crystal. In addition, strong focusing shortens the confocal parameter causing fast divergence and inefficient use of the crystal. In 1964, Boyd and Kleinman [12] calculated the focusing condition for maximum conversion efficiency. They found that the optimal focusing satisfies the following equation

$$\xi = 2.84 = \frac{l_p}{b_c} \tag{2.15}$$

where l_p is length of the optical path of light in the crystal and b_c is the confocal parameter. Consequentially, the optimum waist size is given by

$$w_{opt}^2 = \frac{n_\omega L\lambda}{2\pi 2.84} \tag{2.16}$$

where L is the crystal length. For our wavelength 795 nm and the PPKTP crystal length of $L = 10$ mm the optimum waist is w_{opt}=28μm. Boyd and Kleinman obtained the optimal focusing value by calculating the power conversion efficiency. They found that the conversion efficiency is directly proportional to the

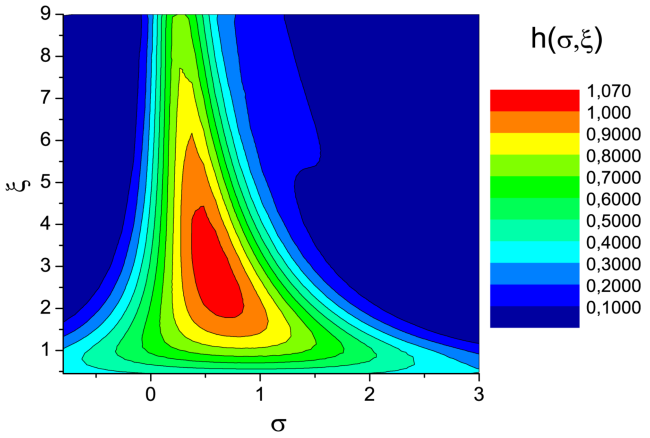

Figure 2.5: The Boyd and Kleinman $h(\sigma,\xi)$ function showing (colored red) the area of maximum conversion.

following function

$$h(\sigma,\xi)=\frac{1}{2\sqrt{\pi}\xi}\int_{-\infty}^{\infty}e^{-4s^2}\left|\int_{-\xi}^{\xi}\frac{e^{i\sigma\tau}}{1+i\tau}d\tau\right|^2 ds. \tag{2.17}$$

Here $\sigma=\frac{1}{2}b\Delta k$ is the wavevector mismatch factor. The function $h(\sigma,\xi)$ is plotted in Figure 2.5. It shows that this function has a maximum for ξ=2.84. Nonetheless, the maximum is rather broad. This allows for conversion close to the maximum with less strong focusing. Defocusing decreases the heating of the illuminated part of the crystal and consequentially decreases the thermal effects in the cavity too. This approach was presented and experimentally confirmed in [42].

Irregular heating of the crystal can cause thermal lensing which can lead to thermal instability of the cavity. Thermal lensing is caused by the absorption of the pump beam which increases the temperature in the center of the crystal along the axis of the beam propagation. The absorption causes a temperature gradient in the crystal which creates a refractive index gradient. Consequentially, the crystal behaves as index graded lens. The thermal lensing in PPKTP affected by 461 nm pump beam was carefully studied in [68].

The ABCD matrix for the index graded lens is given in [56]

$$\begin{vmatrix} \cos\left(L\sqrt{\frac{n_2}{n_o}}\right) & \frac{1}{\sqrt{n_2 n_0}}\sin\left(L\sqrt{\frac{n_2}{n_o}}\right) \\ -n_2 n_0 \sin\left(L\sqrt{\frac{n_2}{n_o}}\right) & \cos\left(L\sqrt{\frac{n_2}{n_o}}\right) \end{vmatrix} \tag{2.18}$$

here n_0 is the refractive index in the center of the crystal and $n_2=n_0\alpha^2$, where α is the pitch [56] of the index graded lens. The expression for n_2 as given in [42] is

$$n_2=\beta_t\frac{\alpha_\omega P}{\pi K_c w_0^2} \tag{2.19}$$

where $\beta_t=\left(n_{301K}-n_{300K}\right)/1K$, α_ω the absorption of the sample, P the applied optical power, $K_c=3.3\,W/mK$ and w_0 waist size. The measurements per-

formed on different PPKTP samples showed that the linear absorption changes very much from sample to sample [25]. In course of design of the cavity we took into account the possibility of existence of thermal lensing. In the theoretical modeling of the possible thermal lensing we used the absorption value cited by [42] for wavelength of 423 nm and which is α_{423nm} =0.1 cm^{-1}. Since the PPKTP transparency range has an edge close to 400 nm depending on the sample, for the wavelength of 397 nm absorption can be considerably larger than for 423 nm. Applying the same treatment of the thermal lensing as presented in [42] we calculated the strength of the thermal lensing assuming the input power of the pump beam to be 100 mW. The temperature change induced by the pump beam to the central of the crystal is according to [42] equal to

$$\Delta T = \frac{\alpha_\omega P}{4\pi K_c}[0.57 + \ln\left(\frac{2r_0^2}{w_0^2}\right)]. \tag{2.20}$$

Modeling the strength of thermal lensing for two different sizes of the focus 42 μm (focus size in our OPO) and 21 μm we found that they have a pitch of the lens 17.2 $m^{-1}$and 35.26 m^{-1}, respectively. This leads to the conclusion that with the doubling the size of the beam the effect of thermal lensing decreases by half. Final design of the cavity as mentioned in section 2.1.1 resulted in the waist of 42 μm which is 50% larger than the Boyd and Kleinman optimum value.

With this geometry (waist of 42 μm) we measured and compared the profile of the counter propagating beam (which cannot experience parametric amplification) without pump light and with the pump present. We noticed no change in the profile which means no thermal lensing effect.

2.1.4 Losses in the cavity and gray tracking

Based on the calculation given in [16] a simple measurement can determine the losses in the cavity. Appendix B.1 describes the calculation in detail. The measurement consists of scanning the cavity length and detecting the light reflected off the cavity. The reflected light signal shows dips in the DC level where the piezo-electric transducer scans over the resonance(s) of the cavity. An example of this signal is shown in Figure 2.6.

If we normalize the reflected power when the cavity is on the resonance P_a to the power reflected when the light is not resonant to the cavity P_b, we can calculate the intracavity losses from the following equation:

$$T_2 = T_1 \cdot \frac{1-R}{1+R} \tag{2.21}$$

where $R = \sqrt{P_a/P_b}$ and T_1 =7.8% is the transmission of the output coupler.

The oscilloscope trace of this measurement is shown in Figure 2.6. The losses in the cavity containing the crystal are 0.50%, excluding the output coupler loss. The intracavity losses change in the presence of the blue pump beam due to the effect known as gray-tracking. The gray-tracking changes the optical properties of the KTP crystal when the crystal is illuminated by visible light beam. The mechanism of gray tracking is not quite clear but a possible explanation is based on the trapping of the holes and electrons by Fe (impurity) and Ti ions, respectively [10]. On the other hand the manifestation of gray-tracking is well known, usually very transparent in the IR region KTP (and also PPKTP) starts to exhibit an increased level of absorption after being exposed to the pump beam.

Gray-tracking is a reversible process, which means that the crystal can recover from the damage. The time of recovery will depend on the power and focusing used during the exposure and it can last from a couple of hours to one year for strong focusing. Low power exposure does not leave visible marks on the crystal but high power tightly focused beams can leave gray color trace along the beam trajectory. These marks need long time to disappear on their own and the crystal in this case rather demands an active healing treatment known as thermal annealing [47].

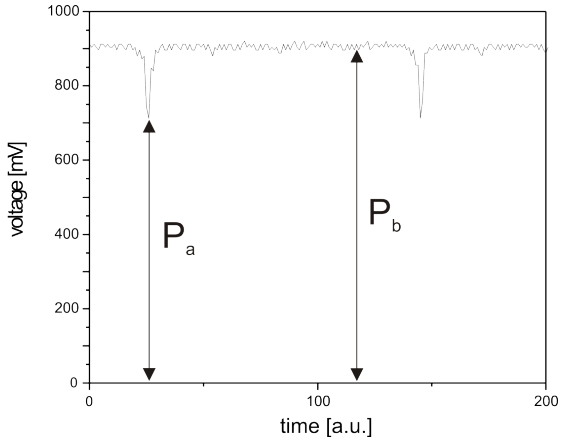

Figure 2.6: Reflection off the OPO cavity, trace taken by the oscilloscope during scanning. The light is injected through the output coupler. The y-axis shows the voltage of the diode detecting the reflected light while the cavity length is being scanned. The voltage ratio between on and off resonance is equal to the ratio of the light power on and off resonance.

The investigations by [8, 10, 9, 19, 69] have shown that the transparency of the crystal changes after the exposure to the blue pump beam. Above mentioned papers measure the absorption after the exposure. None of the above mentioned papers shows the level of absorption while the pump beam is present. We will show here such a measurement using a counter propagating IR beam which in contrary to a co-propagating beam cannot experience parametric amplification. The results are shown in the Figure 2.7. The measurements show that the absorption increases but not on the level as described in [8, 10, 9, 19, 69]. Our measurements were performed on the crystal which was not illuminated by blue light for more than 4 days before. Furthermore, the measurements performed on this crystal are not involving high power beams. Thus, it is reasonable to assume that during this healing time the crystal recovered sufficiently from possible previously induced damage.

The first measurement revealed overall intracavity losses of 0.50% (Figure 2.6). In the following step we illuminated the crystal with the blue pump beam for 30 s measuring simultaneously the losses (Figure 2.7a). The losses increased to 0.515%. After 30 s of exposure we blocked the blue beam and measured the losses again (Figure 2.7b). Now, we observed losses of 1.10%, showing an increase of 0.60% compared with the initial measurement.

We repeated the measurement with the crystal exposed to the blue light

(Figure 2.7c). The losses dropped again to the value close to the one that we had during the first exposure to the blue light. We repeated also the measurements after the exposure (Figure 2.7d). The level of losses was now close to 1.20%.

Obviously the losses in the cavity are reduced during the illumination with the blue light, which is exactly the condition we have for the production of squeezed light.

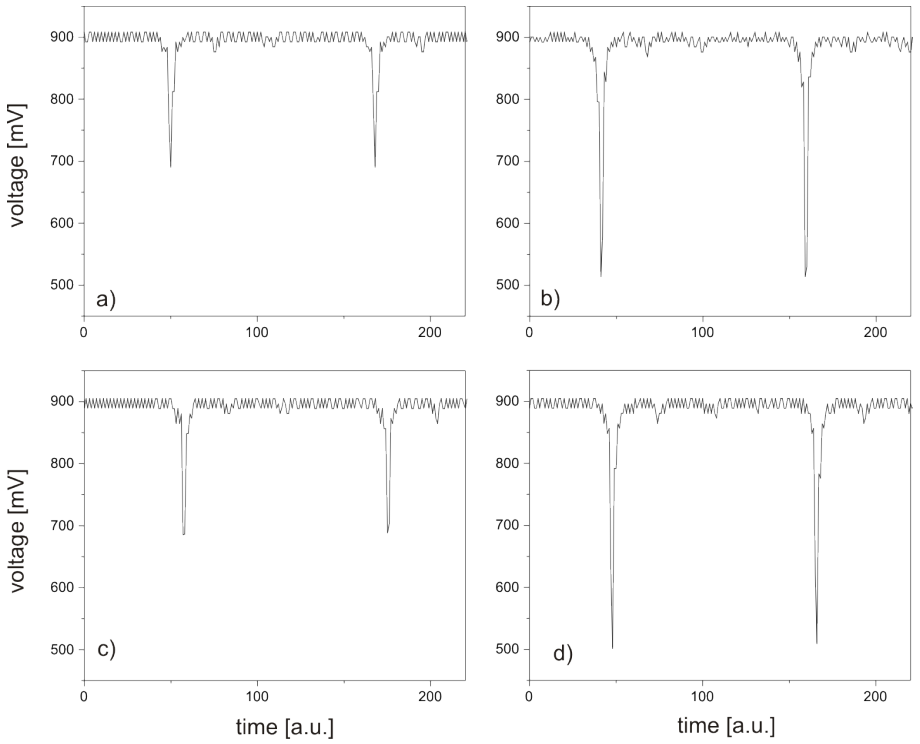

Figure 2.7: The measurements (similar to the one explained on Figure 2.6) of the losses on gray tracking performed on our cavity: a) reflection of the OPO cavity while the crystal is illuminated for the first time with the blue pump b) after 30 s of exposure to the pump light we switch off the pump light and make the measurment c) we again illuminate the cavity for another 30 s (while we make the measurement) d) the masurement taken after second exposure to the blue light.

The results presented on the Figure 2.7 were made with a horizontally polarized pump beam. We made same measurements with the vertically polarized pump beam. The results were similar.

The losses in the cavity after several hours of illumination with blue light were measured (with blue light present) in several occasions, including the same day the presented data was taken. We then measured the losses in the cavity to be 0.55%.

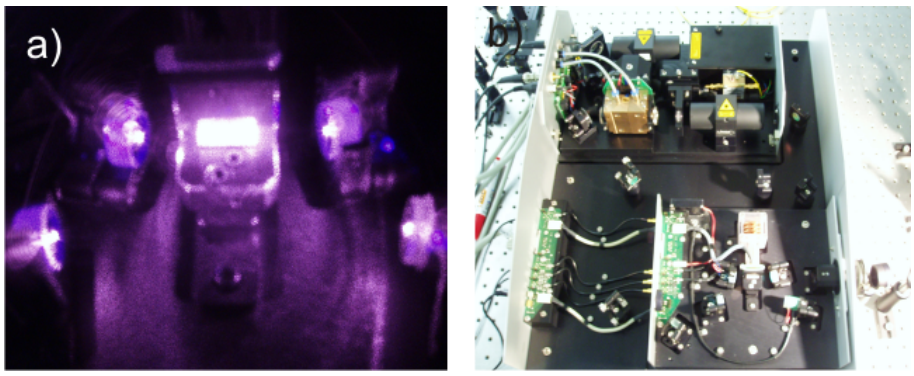

Figure 2.8: a) The generation of the blue light in the doubling cavity b) inside of Toptica TA-SHG; clearly visible two blocks one containing the grating stabilised diode laser with the tapered amplifier and other one containing the doubling cavity.

2.2 Laser system

Our laser system (Toptica TA-SHG) consists of an external-cavity diode laser in Littrow configuration which is amplified by an optical tapered amplifier and a frequency doubler with lithium triborate crystal (LBO) as nonlinear medium. It is shown in the Figure 2.8b. The output of the diode laser is 50 mW before the optical isolator and 35 mW after the isolator. A fraction beam after the isolator (4 mW) passes though a partially reflective mirror. In the experiment this beam is used as local oscillator. The rest of the light is reflected of the mirror and sent into tapered amplifier. The tapered amplifier has an output of 500 mW before the isolator and 400 mW after the optical isolator.

The current driving the diode laser is when it is running optimally 106 mA. The threshold is on 21 mA. Good alignment of the grating on the laser head can give more then 30 GHz mode hop free scanning range. The current on the tapered amplifier chip is 2.1 A at its full power (500 mW before the isolator).

The output of the tapered amplifier is modematched to the doubling cavity. It is a bow-tie cavity of linewidth 14 MHz (shown in Figure 2.8.a). The distance between the curved mirrors is 47 mm, the crystal length is 14 mm and the index of refraction of the LBO crystal is 1.6. The rest of the complete roundtrip is around 220 mm. The incoupling mirror has a reflectivity of 98.5% and the reflectivity of the faces of the crystals should be smaller than 0.25% (according to the manufacturer). The measured losses of the cavity, input coupler excluded are 0.5%. The output of the cavity has the power of more than 130 mW but the mode quality is quite bad. The reason for this is the presence of walk-off in the LBO crystal. The coupling efficiency of cavity output in the single mode fibre is in our case about 60%.

2.2.1 FPGA

Field-Programmable Gate Array (FPGA) is a device which can be programmed to execute logic operations and calculations. FPGA is a "real-time" system executing deterministic operations (each process at well-defined time) there-

fore perfectly suited for control loops. The use of digital electronics for the stabilisation allows for a more flexible and complex controller. Thus, it can be better adapted to the physical system so that is even possible to lock the system across the mechanical resonances. Even more, the system can be automatically (re)locked by the controller. This makes it very stable and easy to operate.

FPGA (National Instruments NI 7833R) we use is relatively easy programmed in Labview, thus does not require complex VHDL programming. It has 8 analog input channels with 200 kHz sampling rate and 8 analog outputs with 1 MHz sampling rate. Three million gates of the FPGA are sufficient to programme 4 of our PID control loops. The FPGA itself is operated at a clock speed of 40 MHz. However, the controller speed is limited by the ADC sampling rate to 200 kHz. Even this speed is faster then required, since the laser stabilisation only feeds back to the grating of the diode laser with a resonance'frequency below 1 kHz of the piezo actuator. Therefore, the controller bandwidth is further limited by a 5 kHz in-loop low pass filter programmed in the FPGA in order to reduce the effect of high-frequency noise.

In everyday operation we set the PID parameters according to the Ziegler-Nichols rules [5, 49]. In practice these rules are used in the following way. First, the set point, i.e. the point to which we want to lock, can be determined visually, looking at the error signal and introduced manually into the control programme. We lock initially using only the proportional part. Then we increase the gain of the proportional part until we observe oscillation. This critical gain value, Ku, and the period of oscillation, Tu, define the optimum parameters according to the standard Ziegler-Nichols rules. In this way the gain parameter of the proportional part, Kp, and the time constants of integral and differential parts, Ti and Td respectively, are set to:

P	I	D
Kp = 0.6 Ku	Ti = 0.5 Tu	Td =0.125 Tu

Once the optimum locking parameters are adjusted and under the condition that the shape and the size of the error signal do not change the re-locking can be performed automatically by the FPGA programme. Another important feature of the FPGA is that it allows us programming some simple signal analysis. For example we use our FPGA to measure the linewidth of the lock while it is locking. The methods used for the linewidth measurement and for obtaining the error signal for locking are explained below in section 2.2.2.

2.2.2 Locking system and linewidth of the laser

The Pound-Drever-Hall technique (PDH) [7] is used to generate the error signals for locking the laser to the doubling cavity, as-well-as for locking the doubling and OPO cavities to the laser. For this purpose a 20 MHz modulation is applied to the laser current, resulting in phase modulation sidebands of 5%. The 20 MHz oscillator signal is distributed to all locking circuits to serve as a reference for demodulation.

The laser and the doubling cavity are locked in frequency with respect to each other. The reflection signal from the doubling cavity is demodulated with the 20 MHz reference to provide the PDH error signal for both locks. A slow analogue proportional-integral-derivative (PID) circuit then acts on the cavity

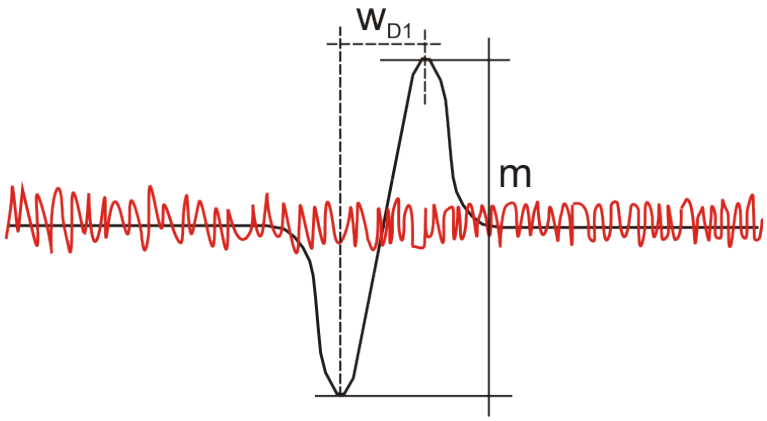

Figure 2.9: Schematic of the error signal. Shown in black line error signal while the absorption feature is being scanned, w_{D1} is the width of the error signal, m is the error signal height peak-to-peak; shown in red line the error signal when the system is locked to the absorption feature which the FPGA uses to calculate the variance Δv_s.

piezo, while a fast proportional component is fed back to the current of the laser diode. Under the assumption that the doubling cavity shows only slow fluctuations the fast feedback reduces the linewidth of the laser, while the slow feedback guarantees that the doubling cavity stays resonant to the laser. The bandwidth of the fast part of this lock is up to 5 MHz.

At the same time, the absolute laser frequency is stabilised by frequency-modulation (FM) spectroscopy of a saturated-absorption signal of rubidium. For the experiments described in this thesis, the laser was locked to the $F = 2 \rightarrow F' = 1$ transition of rubidium-87. The saturated-absorption signal is demodulated with the 20 MHz reference to create the error signal. The locking signal is fed back by a digital PID to the piezo-electric transducer of the grating of the extended cavity diode laser. The digital PID is programmed within the National Instruments FPGA as explained before, see section 2.2.1.

The residual fluctuations of the FM spectroscopy can be used as explained in [54] to measure the linewidth of the laser. Knowing the slope of the error signal it is possible to translate the variance of these fluctuations into a linewidth of the laser. Since the locking signal is obtained by the digital PID circuit, the FPGA was programmed to directly calculate the variance of the error signal of the locked laser. The following formula gives the relation between the variance Δv_s of the error signal and the laser linewidth Δw

$$\Delta w = \Delta v_s w_{D1} m^{-1} \tag{2.22}$$

where $w_{D1} = 5.75\,MHz$ is the width of the D1 transition of rubidium as given in [65] and m is the error signal peak-to-peak size shown in the Figure 2.9. Note that $w_{D1}m^{-1}$ is the slope of the error signal. The results of the linewidth measurements indicate that the fast lock of the doubling cavity reduces the linewidth from 1.2 MHz to 400 kHz full width half maximum (FWHM).

The OPO cavity is locked using a counter-propagating (red) laser beam fed into the cavity through the high reflecting flat mirror. Here, the transmission

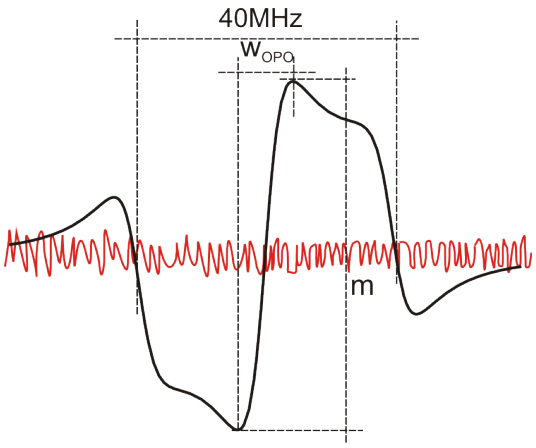

Figure 2.10: Schematic of the error signal. Shown as black line is the error signal when the feature is being scanned, w_{OPO} is the width of the error signal which we can calculate scaling it to the 40 MHz distance between the sidebands, m is the error signal height peak-to-peak; shown as red line is the error signal when the cavity is locked to the transmission which the FPGA uses to calculate the variance Δv_s.

signal is demodulated using the 20 MHz reference signal. The resulting error signal is fed into the digital PID controller. The feedback loop is acting on the piezo-electric transducer which is mounted behind one of the cavity mirrors.

The above mentioned method for characterizing the laser linewidth can be also used to measure the linewidth of the OPO cavity lock using an analogous formula

$$\Delta w_{OPO} = \Delta v_s w_{OPO} m^{-1} \tag{2.23}$$

where the width w_{OPO} of the slope has been calibrated using the fact that the modulation sidebands are 20 MHz from the center, as shown in the Figure 2.10.

We performed the measurement of the linewidth of the OPO lock seeding the locking beam through the output coupler. This method gave us a high quality error signal so that we were able to use to estimate the lower limit of the lock linewidth to 300 kHz. However, under the conditions of the squeezing measurements, the locking signal was too weak to extract a meaningful signal.

2.3 Squeezed light

2.3.1 Parametric gain

The amount of squeezing which can be obtained experimentally, as shown in section 1.3, strongly depends on the available blue pump power (the parameter $\mu = \sqrt{P_\beta (P_\beta^{th})^{-1}}$ is power dependent), as this field is responsible for the parametric gain. The complete calculation for the parametric gain, V, is given in appendix B.3. Here, we will give only the final result

$$V(\mu,\rho) = \frac{P_{out}}{P_1^{in}} = \frac{4k_1k_2}{k^2}\left[\frac{\cos^2\rho}{|1-\mu|^2} + \frac{\sin^2\rho}{|1+\mu|^2}\right]. \tag{2.24}$$

where ρ is the relative phase of the seed field with respect to the pump field.

Experimentally the parametric gain is determined by seeding red light in the OPO cavity and observing the effect the blue pump has on the amplification of the seeded beam. As written in the equation 2.24 the gain, $G(\mu,\rho)$, is equal to the ratio of the output, P_{out}, to input power, P_1^{in}. The parametric amplification is a phase sensitive process and as shown in equation 2.24 it depends on the phase, ρ, between pump field and the seed field. For the experimental characterisation it is easier to compare the output power without blue to the output power with the blue pump field. This gain, $G(\mu,\rho)$, is

$$G(\mu,\rho) = \frac{V(\mu,\rho)}{V(0,\rho)} = \left[\frac{\cos^2\rho}{|1-\mu|^2} + \frac{\sin^2\rho}{|1+\mu|^2}\right]. \tag{2.25}$$

The maximum gain is then achieved for phase $\rho = 0$ with

$$G = (1-\mu)^{-2}. \tag{2.26}$$

The equations 2.24 and 2.25 are calculated in detail in appendix B.3.

A parameter strongly related to the parametric gain is the threshold of the OPO. The threshold is defined as the pump power at which OPO starts to give a classical output. In appendix B.2 is shown that the threshold value depends on the losses in the cavity $(T_1 + T_2)$ and the single pass effective nonlinearity $E_{NL.}$by

$$P_{th} = \frac{(T_1+T_2)^2}{4E_{NL}}. \tag{2.27}$$

The single pass effective nonlinearity of PPKTP is according to literature [34, 42, 68] between 1%/W and 2%/W. Due to low available power (for obtaining 100 μW of blue power we would need approximately 100 mW of red light which was not available from the laser system) we did not measure the single pass nonlinearity of our crystal. If we assume that the crystal's nonlinearity is 1%/W and knowing the output coupler loss is $T_1 = 7.8\%$ and losses in the cavity to be $T_2 = 0.55\%$ we can estimate the threshold power to 180 mW. The threshold power can also be estimated by a second method: in this thesis we measured a maximum gain $G = 3$ at a pump power of $P_\beta = 45$ mW. Using the definition of μ these data set the threshold to be slightly higher, around 250 mW.

2.3.2 Detector

The squeezing was measured with commercially available ThorLabs (PDB150) switchable-gain balanced detector. The quantum efficiency of this detector at detection wavelength of 795 nm is 88% by manufacturer specifications. The low quantum efficiency is mainly caused by the reflection of the surface of the protective window and the photodiode surface. We use two spherical mirrors (R=10 mm), to retro-reflect the reflected light onto the detector improving the quantum efficiency by 7%, i.e., to 95%. Quarter-wave plates are rotating the polarization of the reflected light preventing it in this way to return to the OPO

cavity. The schematic of the detection set-up is shown in Figure 2.11. The focusing of the light onto both photodiodes had to be made with only one lens because the diodes are placed close to each other. Due to this restriction the detection system had to be carefully designed. The care was taken so that the size of the beam on the photodiodes was matching in size. Too small beam would cause saturation of the affected area of the photodiode and too large beam would cause additional losses.

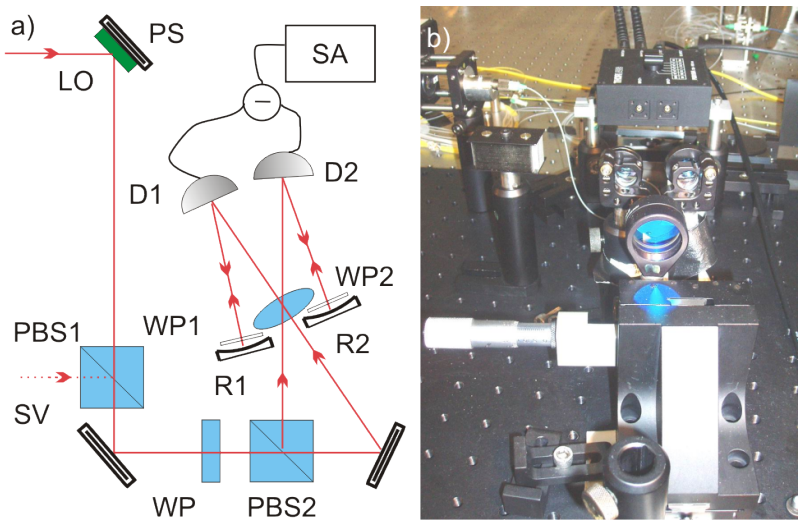

Figure 2.11: The detector set-up. a) schematic of the system: the modes of squeezed vacuum (SV) and local oscillator (LO) are overlapped on a polarising beamsplitter (PBS1); the power balancing is performed by a half waveplate (WP) and a polarising beamsplitter (PBS2) which mix horizontal (LO) and vertical (SV) polarisation ; the light is collected onto diodes D1 and D2 of the balanced detector; the reflections of the diodes surfaces are retroreflected by the spherical mirrors R1 and R2; obtained electrical signal is recorded using a spectrum analyzer (SA); the quarter waveplates WP1 and WP2 are stopping the retroreflected light from entering the locking system by turning the by 90^o degrees in double path b) picture of the detector and the retroreflecting optics mounted on the optical table.

The noise properties of the detector are shown in Figure 2.12. The presented data was obtained in homodyne measurement. The input ports of the homodyne set-up (Figure 2.11) are fed with local oscillator and vacuum, respectively. Practically, this means that in one port of the beamsplitter we sent the laser light and the other one was blocked for light. As in standard balanced homodyne detection the output signal is the difference signal of both photodiodes, therefore amplitude noise of the local oscillator cancels and only the noise due to quantum noise of the light and electronic noise of the detector remains [6]. The output signal is then frequency analysed using a spectrum analyser and measured for different powers of the local oscillator in order to distiguish between the different noise contributions. As written in [6] the electronic noise is independent of the light power, while the quantum noise scales linearly with it:

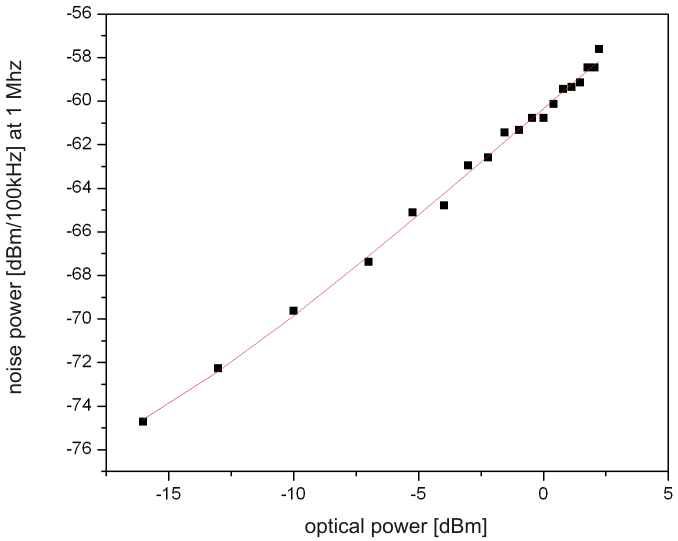

Figure 2.12: Noise power of the homodyne signal for the detection frequency of 1MHz. The red line models the noise contributions as in the equation 2.28.

frequency [MHz]	electronic noise [dBm/100kHz]	linear gain [1/100kHz]
1	-79.3	$9.1\,10^{-7}$
2	-78.5	$8.7\,10^{-7}$
3	-76.6	$8.0\,10^{-7}$
4	-76.3	$6.9\,10^{-7}$
5	-75.0	$5.1\,10^{-7}$

Table 2.2: Electronic noise and the detector gain for different detection frequencies measured with resolution bandwidth of 100 kHz.

$$p_{-}(\nu) = g_{el}(\nu)\, p_i + p_{el}(\nu) \tag{2.28}$$

where p_{-} is the noise power (per resolution bandwidth) of the homodyne signal at the detection frequency ν, p_i is the input optical power, and g_{el} is the linear gain of the detector. The electronic noise (per resolution bandwidth), p_{el}, gives an offset to the homodyne signal.

As shown in Figure 2.12 the equation 2.28 was fitted to the data measured for different powers of the local oscillator, resulting in the electronic noise and linear gain of the detector. The results of the fit are shown in Table 2.2.

2.3.3 Experiment

The schematic of the experiment is shown in the Fig.2.13. As mentioned before in the section 2.2 the laser system (Toptica TA-SHG) consists of the grating

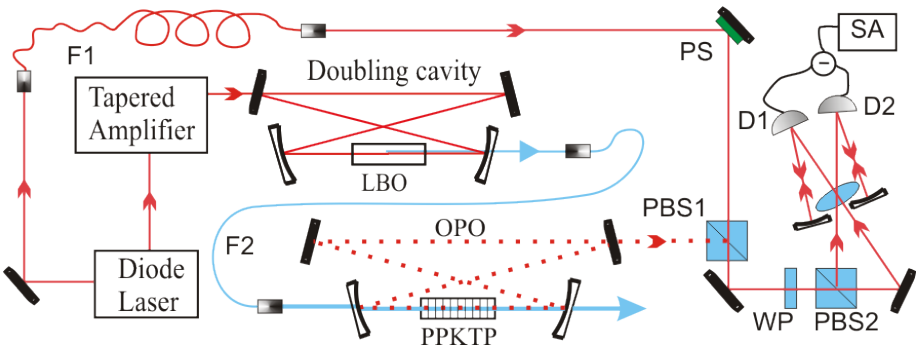

Figure 2.13: Experimental apparatus. Light from the diode laser is amplified in the tapered amplifier and fed into the doubling cavity. The blue output light is mode-matched into fibre F2 and fed into the OPO cavity. Both doubling and OPO cavity are only resonant to the red light. The length of the local oscillator beam path can be changed by fibre F1. The modes of squeezed vacuum and local oscillator are then overlapped on a beamsplitter (PBS1) where power balancing is performed by a waveplate (WP) and a beamsplitter (PBS2). Light is collected onto diodes D1 and D2 of the balanced detector. The obtained electrical signal is recorded using a spectrum analyzer (SA).

stabilised 795 nm diode laser which is amplified by the optical tapered amplifier and injected into the frequency doubler with LBO crystal as the nonlinear medium. The laser is stabilised by frequency-modulation spectroscopy of the saturated-absorption signal, to the $F = 2 \rightarrow F' = 1$ transition of the rubidium-87. Residual fluctuations of the FM spectroscopy signal show that the laser linewidth is 400 kHz full width half maximum (FWHM).

The generated 397 nm light is passed through a single-mode fibre for spatial filtering and pumps the sub-threshold degenerate optical parametric oscillator. The power after the spatial filtering is 45 mW which fed into OPO cavity results in parametric gain of G=3.

Compared to other setups our OPO has a very high cavity escape efficiency which is obtained by appropriate choice of the output coupler and by minimisation of interactivity losses. We have chosen an output coupling mirror of the OPO with a transmission of 7.8%, while the measured interactivity losses are 0.55%. This results in an outcoupling efficiency of $\eta_{OPO} = 0.93$.

For homodyne detection local oscillator light is overlapped with the squeezed light. The local oscillator beam is derived from the diode laser and is passed through a single-mode fibre for spatial mode filtering. The vertically-polarized OPO output is overlapped with 400 μW of this horizontally-polarized beam on polarizing beamsplitter (PBS1). Optimized overlap of these two beams results in measured visibility of close to $VIS = 99\%$. Local oscillator and squeezed vacuum beams are mixed and balanced in power on a second polarizing beamsplitter (PBS2) and detected (with efficiency of $\eta_{det} = 0.95$) with a ThorLabs (PDB150) switchable-gain balanced detector. For the local oscillator power of 400 μW electronic noise of the detector is 14 dB below the standard quantum limit. For all the results presented in this thesis electronic noise was subtracted.

On the path to the detector the squeezing is fragile against losses. If the

squeezed light passes a medium with transmission $\eta < 1$, the medium will change the quadrature variance $V = \langle : q_\theta, q_\theta : \rangle$ of the squeezed light to

$$V' = \eta V + (1 - \eta) \,. \tag{2.29}$$

Therefore losses of the squeezed light should be minimized. The incomplete overlap of local oscillator and squeezed light induces losses which are equal to $\eta_{hom} = VIS^2 = 0.98$. A detailed description of the nature of this loss is given in [11]. The overall losses the squeezed light suffers after leaving the cavity are $1 - \eta = 1 - \eta_{hom}\eta_{pp}\eta_{det} = 1 - 0.86 = 0.14$ or 14%, where $\eta_{pp} = 0.95$ are the propagation losses (losses on reflection off and absorption in optical elements).

As it will be described in the following chapter 3, when fluctuations in frequency are included, the degree of squeezing is expected to depend on the relative delay through two paths: From laser to PBS1 through the local oscillator fibre, and from laser to PBS1 through amplifier, doubler, pump fibre and OPO. Insensitivity to these fluctuations is expected to occur at a "white light" condition of equal delays. We observe the highest level of squeezing of 2.5 dB at the demodulation frequency of 2 MHz which is shown upper part of Figure 2.14 . The squeezing trace shown in Figure 2.14 down is presented here out of pure sentimental reasons. It is the first squeezing trace measured with this OPO and it is very probable to be the first squeezing trace ever taken with a diode pump laser.

All traces are taken with a spectrum analyser. Basically the working principle of the spectrum analyser can be understood as follows. The incoming signal, here the balanced homodyne signal is demodulated at one frequency and filtered by a low-pass filter whose cut-off frequency is set by the resolution bandwidth. Resulting signal is sent into an envelope detector. A second filtering averages over the output signal of the envelope detector. The averaging time of the second filter is set by 1/video bandwidth.

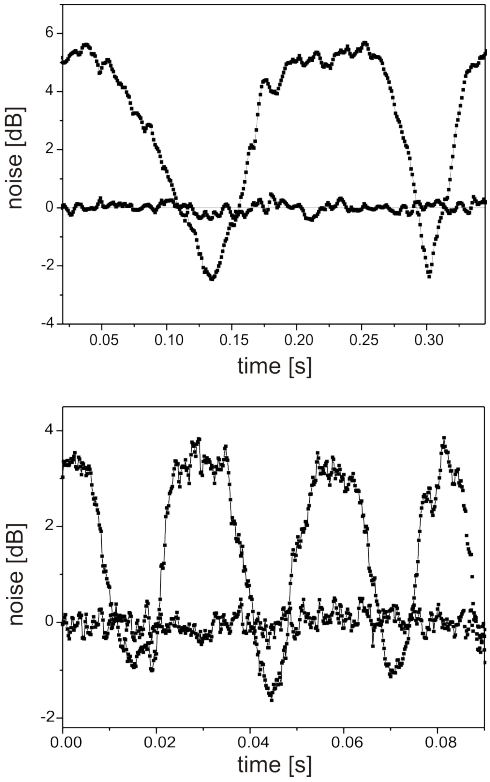

Figure 2.14: Squeezed vacuum generation. Upper figure: (a) squeezing trace when scanning the phase of the local oscillator (b) shot-noise level. Electronic noise is subtracted. Spectrum analyzer at zero span, resolution bandwidth = 30 kHz, video bandwidth = 30 Hz. Lower figure: the first squeezing trace ever taken from our OPO, G=2.5, resolution bandwidth = 300 kHz, video bandwidth = 300 Hz, frequency 3 MHz .

Chapter 3

Compensation of the diode-laser noise

In this chapter we describe a technique to eliminate the effects of laser phase noise on quadrature squeezing. First, in section 3.1 we summarize sources and effects of phase noise in diode lasers. Second, in section 3.2, we derive the observable squeezing produced by the parametric oscillator including the effects of quasi-static frequency fluctuations, and in section 3.4 we show that these can be eliminated by proper choice of local oscillator delay. The sources of delay are explained in detail in section 3.3. We then show in section 3.5 the measurement results: the observed squeezing as a function of delay. With the proper delay, the observed squeezing reaches the level expected from measured characteristics of the OPO and detection system, indicating that the effects of phase noise have been effectively canceled. The technique could also be applied to cancel phase noise in systems not based on diode lasers.

3.1 Diode laser phase noise

Compared to other laser systems, diode lasers are easy to operate, compact, and inexpensive. They allow for tunable operation in a variety of wavelength ranges, so that many important atomic transitions can be addressed. For these reasons, diode-laser-based squeezing would significantly extend the range of possible squeezing experiments. However, it has long been argued that the excess phase noise of the diode laser [76], which results in a relatively large linewidth, would be an obstacle for production of phase-sensitive quantum states such as quadrature squeezing.

The first noise characterisation of diode lasers showed the existence of the phase noise in both free running [52] and grating stabilized [35] diode lasers and it's obvious influence on the light linewidth [48].

The quantum limit for the laser linewidth was calculated by Schawlow and Townes [57]. The outcome is a Lorentzian spectrum with the linewidth given by the Schawlow-Townes formula

$$\Delta\nu_{laser} = \frac{2\pi h\nu_0 \left(\Delta\nu_{1/2}\right)^2 k_{ei}}{P} \tag{3.1}$$

where $h\nu_0$ is the photon energy, $k_{ei} = N_e \left(N_e - N_i\right)^{-1}$ is the parameter describing the population inversion between excited state e and lower state i, $\Delta\nu_{1/2}$ is the full width at half maximum of the passive laser resonator and P is the output power of the laser. Detailed diode laser noise characterisation [20] showed the linewidth to be Lorentzian shaped but 50 times larger than expected. This broadening was explained by Henry [28] as the consequence of the change of the cavity resonance frequency with gain. Henry introduced the linewidth enhancement factor α to quantify this mechanism. Here, α is a proportionality factor relating phase changes to changes of the amplitude gain. Consequently, the linewidth should be increased by a factor of $1 + \alpha^2$, which turned out to be in reasonable agreement with the experimental data.

The broad linewidth can be overcome by making the diode cavity longer (external cavity), thus reducing the linewidth of the passive cavity and the influence of spontaneous emission. This is realized in practice by antireflection coating of the laser output facet and adding a mirror or a diffraction grating as the new output coupler of the extended cavity. This increases the diode laser stability and in case of a diffracion grating adds the ability of tuning the frequency while enforcing single mode operation. In such systems the laser linewidth is now mainly limited by technical imperfections like mechanical vibration of the cavity length.

The spectral properties of external cavity diode lasers were investigated in [37]. There is was shown that the main contribution to the noise comes from the low frequency part of the spectrum. This suggests that the laser output can be treated as quasi-stationary, with the laser frequency drifting slowly (on the time-scale of propagation and cavity relaxation) within the laser linewidth. In [29] the author uses Langevin rate equations of the light field to model the semiconductor laser. The laser is disturbed by fluctuating Langevin forces which change the laser phase. The form of the Langevin force he uses is a Gaussian noise representing the drift of the diode laser external cavity and the spontaneous emission. The equations are solved under assumption of a Markovian system which means that the forces do not depend on their history. The wandering of the phase of the diode laser light represents a phase diffusion of the laser [41] as treated theoretically in [40]. From such calculation the linewidth of the diode laser is expected to be Gaussian shaped [54]. The Gaussian shape result is sustained by the central limit theorem, which states that large number of independent random statistical processes acting on a system results in a normal or Gaussian distribution of the system parameters. Intuitively, the origin of the Gaussian lineshape is a result of a narrow Lorentzian line which due to the vibration of the external cavity is statistically wandering around a central frequency.

3.2 Quasi stationary squeezing theory

In this section the effect of phase noise on the squeezing spectrum will be treated theoretically by adapting the approach of Collet and Gardiner presented previously in section 1.3. The phase fluctuations in the diode laser system result in random frequency fluctuations of the output light. We assume that the frequency drift of the diode laser is slow on the time scale of the decay of light inside the OPO cavity. This is justified as the linewidth of the OPO cavity with

8 MHz is much wider than the linewidth of the laser with 400 kHz.

Here we will calculate the effect these frequency fluctuations have on the squeezing. Our calculation modifies reference [16] by including a relative detuning $\Delta\omega$ between pump laser and OPO cavity caused by the random frequency drifts. The pump light field is still monochromatic only shifted by $\Delta\omega$ from the cavity's central frequency.

As in section 1.3, we start from the quantum Langevin equation of the OPO cavity (equation 1.9)

$$\dot{a} = -\frac{i}{\hbar}[a, H_{sys}] - (k_1 + k_2)\, a + \sqrt{2k_1}a_{v1} + \sqrt{2k_2}a_{v2} \tag{3.2}$$

where as in section 1.3 a and $a^\dagger$ denote the annihilation and creation operators of the cavity mode with frequency ω_0, k_1 and k_2 denote the loss rates through the output coupler and due to intracavity losses, and a_{v1} and a_{v2} denote the annihilation operators of the (vacuum) field entering the cavity due to output coupler and intracavity losses. The Hamiltonian operator of the system as given in equation 1.12 is

$$H_{sys} = \hbar\omega_0 a^\dagger a + \frac{i\hbar}{2}(\varepsilon e^{-i\omega_p t}(a^\dagger)^2 - \varepsilon^* e^{i\omega_p t}a^2). \tag{3.3}$$

After inserting the Hamiltonian into the equation 3.2 we apply the transformation to rotating reference frame $a = \widetilde{a}e^{-i\omega_0 t}$ shifting the zero of the energy scale to the value of $\hbar\omega_0$. Now, we assume that the detuning between the cavity resonance and the pump mode is

$$2\Delta\omega \equiv \omega_p - 2\omega_0 \tag{3.4}$$

We then reach the following equation

$$\dot{\tilde{a}} = \varepsilon e^{-i2\Delta\omega t}\tilde{a}^\dagger - (k_1 + k_2)\,\tilde{a} + \sqrt{2k_1}\tilde{a}_{v1} + \sqrt{2k_2}\tilde{a}_{v2}. \tag{3.5}$$

As in section 1.3 we apply the Fourier transform $(2\pi)^{-\frac{1}{2}}\int dt e^{i\omega t}a\,(t) = a\,(\omega)$ on both sides of the equation 3.5, obtaining

$$\begin{aligned} -i\omega\tilde{a}\,(\omega) \quad &= \quad \varepsilon\tilde{a}^\dagger\,(-\omega + 2\Delta\omega) - (k_1 + k_2)\,\tilde{a}\,(\omega) \\ &\quad +\sqrt{2k_1}\tilde{a}_{v1}\,(\omega) + \sqrt{2k_2}\tilde{a}_{v2}\,(\omega)\,. \end{aligned} \tag{3.6}$$

In order to make the equations more symmetrical we shift the frequency $\omega \to \omega + \Delta\omega$ by which equation 3.6 gets the form

$$\begin{aligned} -i\,(\omega + \Delta\omega)\,\tilde{a}\,(\omega + \Delta\omega) \quad &= \quad \varepsilon\tilde{a}^\dagger\,(-\omega + \Delta\omega) - (k_1 + k_2)\,\tilde{a}\,(\omega + \Delta\omega) \\ &\quad +\sqrt{2k_1}\tilde{a}_{v1}\,(\omega + \Delta\omega) + \sqrt{2k_2}\tilde{a}_{v2}\,(\omega + \Delta\omega)\,. \end{aligned} \tag{3.7}$$

As shown in section 1.3 the equation 3.7 together with its Hermitian conjugate can be solved for the field inside the cavity, $\tilde{a}\,(\omega + \Delta\omega)$ (shown in more detail in the appendix C.1). Using the input-output relation

$$\sqrt{2k_1}\tilde{a}\,(\omega) = \tilde{a}_{v1}\,(\omega) + \tilde{a}_{out}\,(\omega) \tag{3.8}$$

we reach the Bogoliubov transformation from input to output fields

$$\begin{aligned}\tilde{a}_{out}(\omega+\Delta\omega) &= g_1\tilde{a}_{v1}(\omega+\Delta\omega)+g_2\tilde{a}^{\dagger}_{v1}(-\omega+\Delta\omega)\\ &\quad+g_3\tilde{a}_{v2}(\omega+\Delta\omega)\\ &\quad+g_4\tilde{a}^{\dagger}_{v2}(-\omega+\Delta\omega)\end{aligned}\tag{3.9}$$

where

$$g_1 = \left[\eta^2-(1-\eta-i\Omega)^2+\Delta\Omega(2\eta i-\Delta\Omega)+|\mu|^2\right]B_1^{-1}\tag{3.10}$$

$$g_2 = 2\eta\mu B_1^{-1}\tag{3.11}$$

$$g_3 = 2\sqrt{\eta(1-\eta)}\,(i(-\Omega+\Delta\Omega)+1)\,B_1^{-1}\tag{3.12}$$

$$g_4 = 2\mu\sqrt{\eta(1-\eta)}B_1^{-1}\tag{3.13}$$

$$B_1 = (1-i\Omega)^2+\Delta\Omega^2-|\mu|^2.\tag{3.14}$$

Here $\Delta\Omega$, Ω, η and μ are the parameters scaled to the cavity linewidth $\delta\nu = k_1+k_2$ as previosly shown in chapter 1. Details of this calculation are shown in appendix C.1.

We note that the operators for the output field, $\tilde{a}_{out}(\omega+\Delta\omega)$ as in equation 3.9, fulfill the standard commutation relations for bosonic operators.

The squeezing spectrum $S(\Omega)$ can be deduced from equation (3.9) using the definition of the quadrature operator

$$q_\theta = \frac{1}{\sqrt{2}}(\tilde{a}_{out}(\omega+\Delta\omega)\,e^{-i\theta}+\tilde{a}^{\dagger}_{out}(\omega+\Delta\omega)\,e^{i\theta})\tag{3.15}$$

$$\begin{aligned}S(\Omega) &= 1+2\eta_{det}\langle :q_\theta,q_\theta:\rangle\\ &= 1+\frac{8\eta_{det}\eta|\mu|^2}{|B_1|^2}\left[1+\frac{\left(1-\Delta\Omega^2+\Omega^2+|\mu|^2\right)}{2|\mu|}\cos(2\theta-\phi)\right.\\ &\quad\left.+\frac{\Delta\Omega}{|\mu|}\sin(2\theta-\phi)\right].\end{aligned}\tag{3.16}$$

Formula 3.16 in the limit of no detuning from the cavity resonance ($\Delta\Omega = 0$) is equal to the formula 1.43 derived in the section 1.3.

Figure 3.1 shows the squeezing function $S(\Omega)$ versus relative phase between squeezed light and the local oscillator $(2\theta-\phi)$ for the different values of the detuning ($\Delta\Omega$). Depending on the detuning the minimum of the function $S(\Omega)$ (maximum squeezing) will vary in depth. In addition, the minimum corresponds, depending on $\Delta\Omega$, to different values of the relative phase $2\theta-\phi$. If the frequency drift can not be suppressed by means of frequency stabilisation, the drift of the relative phase between the squeezed light and the local oscillator will cause a reduction in the detected amount of squeezing. This can be understood in the following way: The homodyne technique measures the level of noise for the relative phase between local oscillator and squeezed light. If now the relative phase between local oscillator and squeezed mode drifts it will "average" the squeezing level over the angle of the relative phase drift. This situation is

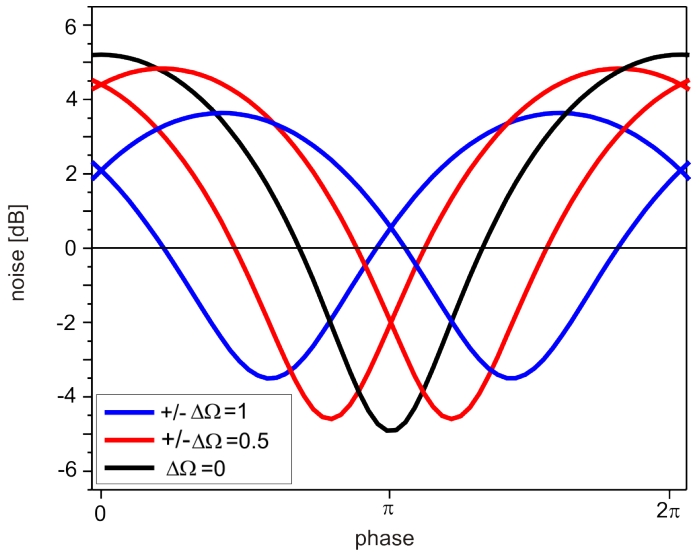

Figure 3.1: Level of noise (squeezing) versus relative phase between squeezed light and the local oscillator for different values of detuning from the cavity resonance scaled to the cavity linewidth ($\Delta\Omega$). The black curve shows the squeezing at the cavity resonance ($\Delta\Omega = 0$). The red and the blue curves show the effect of detuning on squeezing. The red curves represent the detuning of $\Delta\Omega = \pm 0.5$ (left for minus and right for plus). The blue curves represent the detuning of $\Delta\Omega = \pm 1$ (also left for minus and right for plus)

schematically depicted in the figure 3.2. In the figure 3.2 we have chosen on purpose the noisier quadrature due to fact that the process is more obvious on this quadrature. In the following section we will show how to compensate for this averaging effect by making the local oscillator and the squeezed light correlated in phase.

3.3 Delay

As explained previosly in section 3.1 an important characteristics of the diode laser is it's excess phase noise. It shows up predominantly at low frequency and can be understood as a random phase drift. Another way to see this phase drift is as a random laser frequency drift around the central carrier. In the previous section we have shown which effect such detuning from the central line (the resonance of the OPO cavity) has on the quadrature squeezing. In the following we explain our technique to eliminate these negative effects. It employs cavity stabilisation of the laser frequency (alredy explained in detail in section 2.2.2), in combination with a carefully chosen delay of the local oscillator beam.

Complete elimination of the diode laser's frequency drift is a challenging task. Nevertheless, one can overcome this problem by making the experiment insensitive to the frequency drift. In practice this is made by balancing the pathes of the local oscillator and the squeezed beam, thus preserving the correlation of the frequency/phase drifts at the homodyne detection. In the following

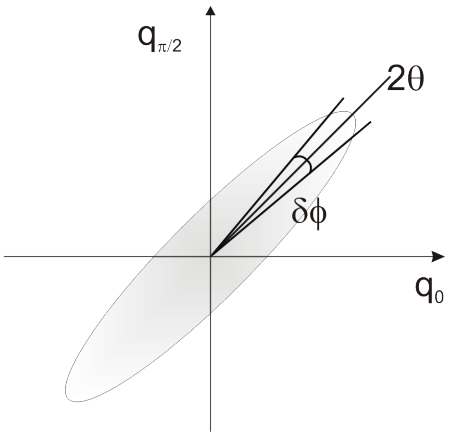

Figure 3.2: The "averaging" of the squeezing level over the angle of the relative phase drift. Here 2θ is the angle of the local oscillator and $\delta\phi$ represents the angle of the relative phase drift.

we first discuss the delay of the light signal for the different components in the squeezing beam path. We will then introduce the same delay into local oscillator path to achieve the required path balance.

First, we introduce τ_D the group delay between the local oscillator and the pump light at the OPO cavity. The delay of the OPO cavity will be discussed later. As both local oscillator and OPO pump are derived from the same laser, we can identify $\tau_D = 0$ as a "white-light" condition in a Mach-Zehnder-topology interferometer. In this "white light" configuration the effect of the frequency drift is expected to be minimum. The light in the squeezing path passes the tapered amplifier, doubling cavity, mode matching fibre, lengths of free-space propagation (and the OPO cavity) as shown in the figure 2.13.

The delay of light for the free space propagation is

$$\tau_{freeprop} = \frac{s}{c} \tag{3.17}$$

where s is the path length of the free propagation and c is the speed of light. The tapered amplifier is contributing with the path length through it. The delay introduced by the doubling cavity is the cavity group delay at line center (for a general formula for arbitrary detuning see appendix C.2)

$$\tau_{doub.cav} = \frac{1}{\pi \cdot \delta\nu}. \tag{3.18}$$

The measured doubling cavity linewidth is $\delta\nu = 14\,\mathrm{MHz}$ which results in the delay of $2.27 \times 10^{-9}\,s$. The mode cleaning fibre for the blue pump of the OPO will introduce the group delay

$$\tau_{bluegroup} = \frac{l_{bf}\left(n_b - \lambda\frac{dn_b}{d\lambda}\right)}{c} \tag{3.19}$$

where l_{bf} is the length of the blue fibre and $n_b = 1.45$ is the index of refraction of the fibre. Since the refractive index does not change significantly this delay can be approximated with the phase delay

$$\tau_{bluef} = \frac{l_{bf} n_b}{c} \tag{3.20}$$

The light in the local oscillator path passes lengths of free-space propagation and a mode-cleaning fibre. The overall delay of the local oscillator is

$$\tau_{lo} = \frac{s_{lo} + l_{lo} n}{c} \tag{3.21}$$

where s_{lo} and l_{lo} are the free space and fibre propagation in the local oscillator path, respectively. The local oscillator light experiences the index of refraction $n = 1.5$ in the fibre. The length of local oscillator mode cleaning fibre can be changed in order to achieve the white light balance of the paths or if necessary additional delay. The delay τ_D is

$$\tau_D = \tau_{lo} - (\tau_{freeprop} + \tau_{doub.cav} + \tau_{bluef}) \tag{3.22}$$

and it is equal to zero in white light configuration. This configuration is achieved when the total delay in the local oscillator path, as calculated from measurements of fibre and free-space lengths, is equal to the combined delays in the amplifier, doubling cavity, fibre and free space. A positive value of τ_D indicates that local oscillator field is delayed with respect to the pump field. We do not include the OPO cavity delay because this depends on demodulation frequency Ω which will be explained later.

3.4 White light

First, we need to analyse the phase shift introduced by a delay line. Starting from the Fourier transform as discussed in the appendix A.1 the temporal dependency of the output field can be expressed as

$$\tilde{a}_{out}(\omega) = \frac{1}{\sqrt{2\pi}} \int dt e^{i\omega t} \tilde{a}_{out}(t) \tag{3.23}$$

$$\tilde{a}_{out}(t) = \frac{1}{\sqrt{2\pi}} \int d\omega e^{-i\omega t} \tilde{a}_{out}(\omega). \tag{3.24}$$

For a delay line without dispersion or absorption the output field will only experience a phase shift with respect to the input field of the form

$$\tilde{a}_{out}(\omega) = f(\omega)\, \tilde{a}_{in}(\omega) \tag{3.25}$$

where the phase shift is linearly dependent on the angular frequency ω, i.e. $f(\omega) = e^{im\omega}$.Replacing this linear dependency into equation 3.24 we obtain the following temporal evolution from input to output field

$$\begin{aligned} \tilde{a}_{out}(t) &= \frac{1}{\sqrt{2\pi}} \int d\omega e^{-i\omega t} e^{im\omega} \tilde{a}_{in}(\omega) \\ &= \frac{1}{\sqrt{2\pi}} \int d\omega e^{-i\omega(t-m)} \tilde{a}_{in}(\omega) \\ &= \tilde{a}_{in}(t-m). \end{aligned} \tag{3.26}$$

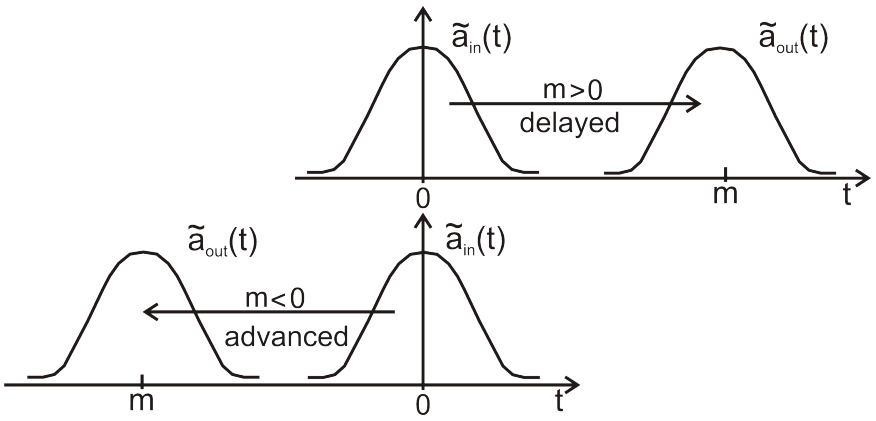

Figure 3.3: Schematic of the advance and the delay of the field

This means that a positive slope of the phase shift, $m > 0$, introduces a delayed output field with respect to the input field, see also figure 3.3. In contrary, a negative slope, $m < 0$, would lead to an advanced output signal. To conclude, in our notation a delay line of delay τ introduces a positive phase shift vs. frequency of the form $f(\omega) = e^{+i\tau\omega}$.

The delay of the local oscillator will therefore induce a positive shift of the phase of the form

$$\theta = \theta_0 + \Delta\omega\tau_{lo}. \tag{3.27}$$

Similarly, the pump beam will experience a phase shift

$$\phi = \phi_0 + 2\Delta\omega(\tau_{freeprop} + \tau_{doub.cav} + \tau_{bluef}). \tag{3.28}$$

Therefore, the total phase as it appears in equation 3.16 takes the form

$$2\theta - \phi = \Delta\phi + 2\Delta\omega\tau_D \tag{3.29}$$

where $\Delta\phi = 2\theta_0 - \phi$ denotes the relative phase between the phase of the local oscillator in the white light configuration and of the pump laser of the OPO, $\mu = |\mu|e^{i\phi}$.

The squeezing spectrum $S(\Omega)$ is

$$\begin{aligned} S(\Omega) &= 1 + 2\eta_{det} \langle : q_\theta, q_\theta : \rangle \\ &= 1 + \frac{8\eta_{det}\eta\,|\mu|^2}{|B_1|^2}\left[1 + \frac{\left(1 - \Delta\Omega^2 + \Omega^2 + |\mu|^2\right)}{2|\mu|}\cos\left(\Delta\phi + 2\Delta\omega\tau_D\right)\right. \\ &\quad \left. + \frac{\Delta\Omega}{|\mu|}\sin\left(\Delta\phi + 2\Delta\omega\tau_D\right)\right]. \end{aligned} \tag{3.30}$$

Best squeezing is obtained for the phase that gives

$$\tan(\Delta\phi + 2\Delta\omega\tau_D) = \frac{2\Delta\Omega}{1 - \Delta\Omega^2 + \Omega^2 + |\mu|^2} \tag{3.31}$$

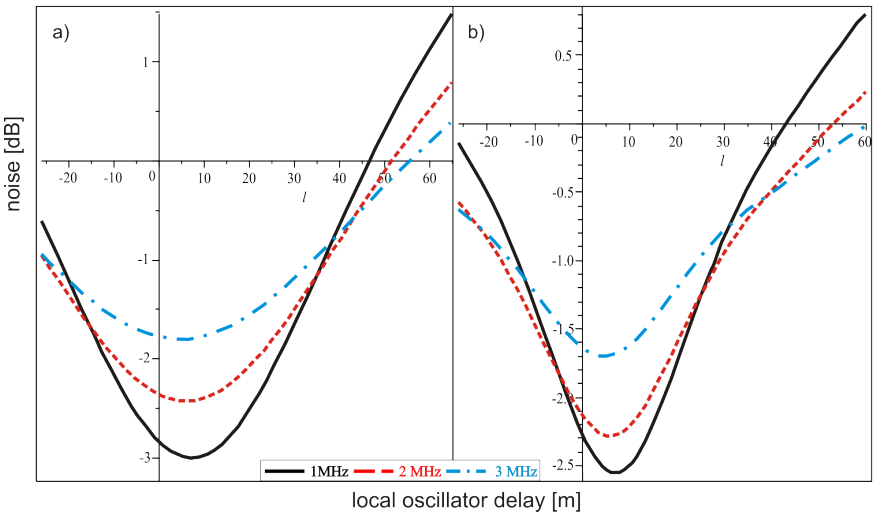

Figure 3.4: Squeezing vs.delay for three different detection frequencies 1 MHz, 2 MHz, and 3 MHz depicted black (solid), red (dashed), and blue (dot-dashed), respectively; a) models the laser spectrum as Gaussian of linewidth 700 kHz full width half maximum (FWHM), b) models the laser spectrum as Lorentzian of linewidth 300 kHz (FWHM).

which due to the cavity dispersion depends on the detuning of the pump laser $\Delta\Omega$. The right side of the equation represents the delay in the OPO cavity which was not included in the previously discussed delays. In first order of the detuning the squeezing phase is

$$\Delta\phi + 2\Delta\omega\tau_D = \pi + \frac{2}{1+\Omega^2+|\mu|^2}\Delta\Omega. \tag{3.32}$$

This dispersion can be compensated by delaying the local oscillator before the homodyne detection. A delay line of length l and refractive index n of the fibre will introduce the phase shift

$$2\Delta\omega\tau_D = 2(k_1+k_2)\frac{ln}{c}\Delta\Omega. \tag{3.33}$$

Thus for the additional delay length of the local oscillator

$$l = \frac{c}{n(k_1+k_2)(1+\Omega^2+|\mu|^2)} \tag{3.34}$$

the homodyne detection will be performed, to first order, at the correct squeezing phase $\Delta\phi = \pi$ even for detuned pump. The dispersion in the OPO cavity and therefore also the compensation length depends on the detection frequency Ω. For higher detection frequency a shorter compensation delay is necessary. Note that the delay presented here is not equivalent to the classical delay as shown in appendix C.2 although they both depend on the detuning. The main difference is that the delay within the OPO cavity depends on the gain and the demodulation frequency.

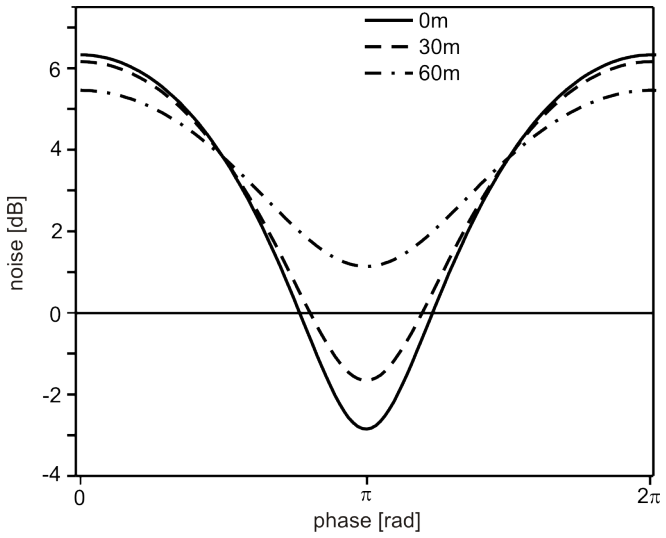

Figure 3.5: Squeezing versus phase for three different delay lengths l= {0,30,60} m, solid, dashed, dot-dashed line, respectively. The parameters used to plot these curves are equal to the experimental parameters given in section 2.3.3. The demodulation frequency used is 1 MHz.

The calculation above was conducted under the assumption of monochromatic light. Nevertheless, in a real system the detuning is not a constant, but the frequency drifts within a certain range. We here assume that slow frequency drift has a power spectral density of $\rho(\Delta\Omega)d\Delta\Omega$. The measurable squeezing signal is obtained by averaging the homodyne power spectrum $S(\Omega)$ over $\Delta\Omega$. The averaged squeezing spectrum is then given by

$$\bar{S}(\Omega) = \int_{-\infty}^{+\infty} S(\Omega)\rho(\Delta\Omega)\, d\Delta\Omega. \tag{3.35}$$

We note that the homodyne power spectrum$S(\Omega)$ is a function also of $\Delta\Omega$, l and many other parameters. The $\bar{S}(\Omega)$ dependency on the delay length l is plotted in Fig.3.4 for a Gaussian and a Lorentzian linewidth $\rho(\Delta\Omega)$.

On the figure 3.4 we see the shift of optimum squeezing to positive delay due to the delay introduced by OPO, as given in equation 3.34. As discussed above the shift depends on the demodulation frequency. As the frequency drift spectral density is a symmetrical function the optimum squeezing is observed for $\Delta\phi = \pi$ as plotted in figure 3.5.

3.5 Experiment

Here we present the experimental investigation of the theory presented in the previous sections. The set-up is explained in section 2.3.3. The mode cleaning fibre F_1 depicted in the figure 2.13 was used to vary the path-length of the local oscillator field.

We have performed a series of measurement where this delay was introduced in the path of the local oscillator with intention to: (i) measure the level of

squeezing in white light configuration (results presented in the section 2.3.3) (ii) see the effect of the change of delay on the level of squeezing. The results are presented in the figure 3.6. The experimental paremeters: gain, losses etc. are the same as presented in the section 2.3.3.

We measured the quadrature variance for every four meters added in the local oscillator path starting from the proximity of the balanced (white light) configuration. Final fibre length was 60 m longer than the balanced configuration. Due to the limited pump power and large fibre losses for the blue light measurements at negative delay were not feasible. For every 4 m of delay we placed in the local oscillator path we performed several measurements of the quadrature variance (squeezing). Then we averaged the obtained level of squeezing over several taken traces. The average values and their standard deviation (vertical error bars) for every length are plotted in the figure 3.6. The figure shows the measured squeezing vs. delay for three different demodulation frequencies 1 MHz, 2 MHz and 3 MHz (Fig. 3.6). The experimental results show minima at positive delay as predicted by theory. Equation 3.34 predicts $l = \{7.3, 6.0, 4.7\}$ m shift for demodulation frequencies $\{1, 2, 3\}$ MHz, respectively.

The theoretical curves in figure 3.6 are obtained using all experimental parameters as stated above, but varying the width of $\rho(\Delta\Omega)$ as the only free parameter. Of two different profiles treated in the theory the comparison with the Gaussian reflects the shape of the experimental curve more closely than the Lorentzian profile. We see good agreement, especially at 3 MHz demodulation frequency, for a Gaussian spectrum of 700 kHz (FWHM). The better of agreement of the Gaussian shaped profile was to be expected by the central limit theorem, see section 3.1. We note that physically $\Delta\Omega$ is the mismatch between half the pump frequency and the OPO cavity frequency scaled to the cavity linewidth, and thus both laser frequency fluctuations and OPO cavity fluctuations will contribute to $\rho(\Delta\Omega)$. Using the in-loop signal from the laser lock to a saturated-absorption reference, we find a 400 kHz laser linewidth (shown in detail in section 2.2.2). A similar measurement of the distribution of $\omega_0 - \omega_{laser}$ can be made using the OPO cavity locking signal. Under the conditions of the squeezing measurements, however, the locking signal was too weak to extract a meaningful signal, largely because we cannot inject through the output mirror as in the PDH technique. We can place a lower limit of 300 kHz on the width of $\rho(\Delta\Omega)$ based on PDH locking of the same cavity, and the 700 kHz estimate for the width of $\rho(\Delta\Omega)$ appears reasonable.

On the other hand, the level of squeezing we observe in the 1 MHz and 2 MHz measurements is smaller than predicted by theory. This might be caused by the light back reflected form the end faces of the nonlinear crystal contaminating the squeezed light. If we assume that this noise is independent of the relative delay, it can be modeled by a constant offset to our theoretical squeezing curves. With an offset of (+0.07,+0.03) relative to the standard quantum limit for (1, 2) MHz, respectively, the theory for a Gaussian laser spectrum of 700 kHz fits well in shape and amplitude to our measured data as shown in fig. 3.6.

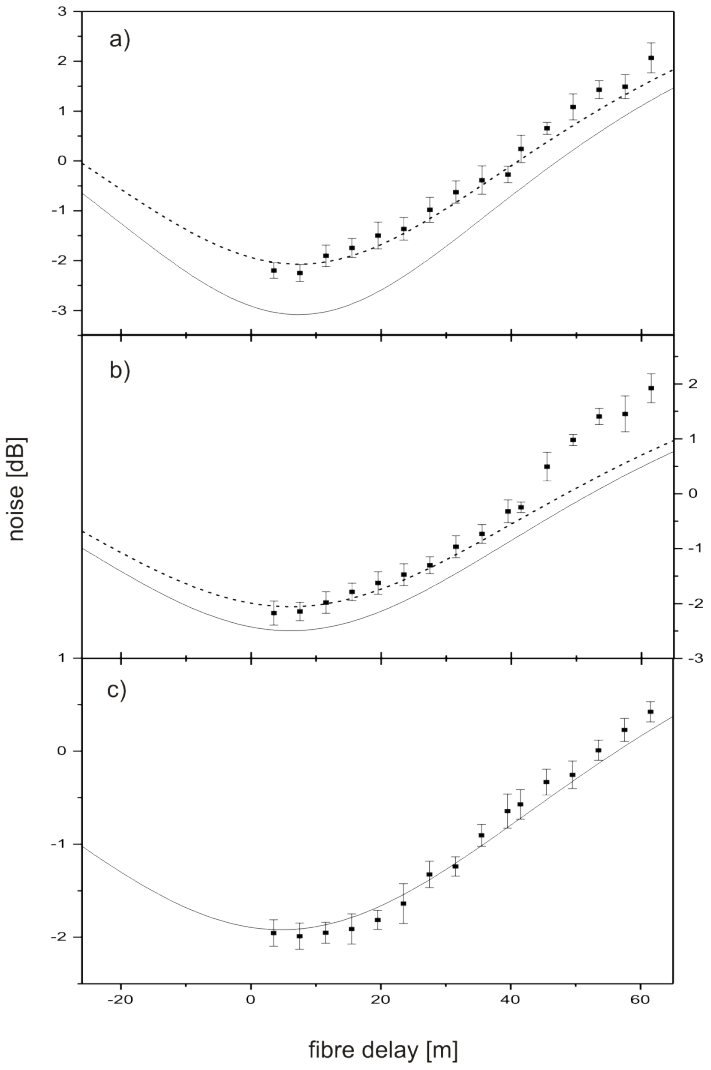

Figure 3.6: Squeezing dependent on the path mismatch measured for three different detection (demodulation) frequencies: a) 1 MHz, b) 2 MHz c) 3 MHz. The points show the experimental data, the solid lines the predicted level of squeezing for the parameters measured in the experiments using a Gaussian profile of 700 kHz linewidth (FWHM), the dashed lines show the theoretical level of squeezing for the same parameters as the solid line with additional technical noise independent of the relative delay. The error bars represent standard deviation over series of identical measurements.

Chapter 4

Conclusions

We have shown in this thesis a technique for generation of quadrature (and polarisation) squeezing using a sub-threshold OPO and a frequency-doubled diode laser as a pump. The pump system consists of external cavity diode laser whose output is amplified in an semiconductor tapered amplifier and fed into doubling cavity with LBO as nonlinear medium. The frequency-doubled light pumps the OPO cavity which is 60cm long, in bow-tie geometry, and with PPKTP as nonlinear medium. The generated squeezed light was resonant to the Rubidium D1 transition as the primary diode laser was locked to the saturated absorption line of the atomic resonance. The locking of the laser to the atomic transition of rubidium as well as the locking of the doubling and the OPO cavity were performed by the Pound-Drever-Hall technique. The control of the locking feedback was performed by a PID (Proportional Integrative Derivative) circuit synthesised onto an FPGA (Field Programmable Gate Array) board. The output of the OPO is analysed by homodyne detection with the primary diode laser as the local oscillator. The detection efficiency was improved by retroreflection of the lost light back onto the diode. The maximum squeezing achieved in the experiment was 2.5dB below shot-noise level. This result is consistent with the measured losses in the cavity, parametric gain and overall detection efficiency. Moreover, we have analysed the effect of the diode lasers phase noise onto the squeezing generated by such a system. For a phase noise affected system we expected that the squeezing level would depend on the relative delay between squeezing and local oscillator path. This effect was experimentally confirmed as optimum squeezing was observed for white light configuration.

For the theoretical description of this effect we adapted the monochromatic treatment of Collet and Gardiner as given in [16] taking into account the phase noise of the diode laser. Such noise mainly leads to low frequency contributions in the spectrum. Under this assumption we were able to treat the diode laser output as quasi-stationary, with the laser frequency drifting slowly (on the time-scale of propagation and cavity relaxation) within the laser linewidth. Our theoretical description accounts for any relative frequency deviation of pump laser vs. OPO cavity, thus it includes the random frequency fluctuations of the pump laser but also of the stabilized OPO cavity. The theory predicts that the phase sensitive amplification of vacuum in the OPO cavity shows a dispersive behaviour where the dispersion depends on the detection frequency of the squeezing. The resulting group delay is equivalent to between 4.7m (3MHz) and

7.3m (1MHz) of fibre delay line. The experimental results confirmed this theoretical prediction and thus demonstrated that the vacuum mode of the OPO is indeed taking part in the delay line. The dependence of the squeezing level on the delay was also predicted by this theory. Experiment and theory were consistent for a relative linewidth of pump laser vs. OPO cavity of approximately 700kHz for a Gaussian spectrum.

In short, we have both theoretically and experimentally investigated and optimized the squeezing properties by using a delayed local oscillator. Using appropriate delay of the local oscillator it is possible to make the quadrature squeezing immune to the random frequency drifts which makes diode laser squeezing possible and a useful resource for future quantum memory experiments.

Outlook

Squeezing with diode sources brings many applications into reach which would not be possible with complicated solid state or dye lasers. Compared to these, diode lasers have many advantages: They are robust, much cheaper and simpler to operate, are available for many frequencies from UV to IR, and often allow tunable operation over a large wavelength range. Many atomic transitions can be addressed by diode lasers. Now all these advantages are directly available for new squeezing devices. Their broad spectral coverage will make diode laser squeezing a useful resource for future quantum memory experiments on new atomic species. Moreover, compact, robust and cheaper squeezing devices could be used as a versatile tool for precise measurements. Size and robustness could pave the way for applications in space, e.g. for high-sensitivity gravitational wave detection. It seems even possible to combine all the building blocks on a chip which would allow for miniaturised squeezing devices.

Appendix A

Quantum theory of the OPO

This appendix gives the details necessary for the calculation of the squeezing spectrum. We give in section A.1 the definition of the Fourier transform as it is used throughout the thesis. Later in section A.2 we give the mathematical definition of the covariance (variance) and show that in case of coherent state only antinormlly ordered variances are not equal to zero.

A.1 Fourier transform

The Fourier transform of the time dependent annihilation operator $a(t)$ is

$$F\left[a\left(t\right)\right]=a\left(\omega\right). \tag{A.1}$$

It can be calculated in the following way

$$\frac{1}{\sqrt{2\pi}}\int dte^{i\omega t}a\left(t\right)=a\left(\omega\right)\longleftrightarrow a\left(t\right)=\frac{1}{\sqrt{2\pi}}\int dte^{-i\omega t}a\left(\omega\right). \tag{A.2}$$

From this relation we can deduce a relation for the hermitian conjugates of the annihilation operator in time and frequency space. We can form the hermitian conjugate of the previous equation and obtain

$$\left[a\left(t\right)\right]^{\dagger}=\frac{1}{\sqrt{2\pi}}\left[\int d\omega e^{-i\omega t}a\left(\omega\right)\right]^{\dagger} \tag{A.3}$$

or

$$\left[a\left(t\right)\right]^{\dagger}=\frac{1}{\sqrt{2\pi}}\int d\omega e^{i\omega t}a^{\dagger}\left(\omega\right). \tag{A.4}$$

The inverse equation is then

$$\left[a\left(\omega\right)\right]^{\dagger}=\frac{1}{\sqrt{2\pi}}\int dte^{-i\omega t}a^{\dagger}\left(t\right) \tag{A.5}$$

which results in

$$F\left[a^{\dagger}\left(t\right)\right]=a^{\dagger}\left(-\omega\right). \tag{A.6}$$

Note that the Fourier transform of the time dependent creation operator is the creation operation in frequency space but with negative frequency.

A.2 Covariance and normal ordering

The definition of the covariance for two operators A and B is:

$$\langle A, B\rangle = \langle AB\rangle - \langle A\rangle \langle B\rangle . \tag{A.7}$$

The covariance has the properties

$$\langle A, B\rangle = \langle [A, B]\rangle + \langle B, A\rangle . \tag{A.8}$$

and

$$\begin{aligned} \left\langle A^\dagger, B^\dagger\right\rangle &= \left\langle A^\dagger B^\dagger\right\rangle - \left\langle A^\dagger\right\rangle \left\langle B^\dagger\right\rangle \\ &= \left\langle (BA)^\dagger\right\rangle - \langle A\rangle^* \langle B\rangle^* \\ &= \langle A, B\rangle^* . \end{aligned} \tag{A.9}$$

In the following we want to calculate the covariance for the coherence/vacuum state as it is needed in chapter 1 for the calculation of the squeezing spectrum. Here $a(\omega)$ and $a^\dagger(\omega)$ are annihilation and creation operators of the input field of the OPO cavity at frequency ω which fulfill the relation $\left[a(\omega), a^\dagger(\omega')\right] = \delta(\omega - \omega')$ and$|\alpha\rangle$ is a coherent state, the eigenstate of the annihilation operator $a(\omega)$ with eigenvalue $\alpha(\omega)$. We will now calculate the covariances for the coherent/vacuum state. For the annihilation operators we get

$$\begin{aligned} \langle a(\omega)\,,\, a(\omega')\rangle &= \langle \alpha |a(\omega)\, a(\omega')| \alpha\rangle - \langle \alpha |a(\omega)| \alpha\rangle \langle \alpha |a(\omega')| \alpha\rangle \\ &= \alpha(\omega)\alpha(\omega') - \alpha(\omega)\,\alpha(\omega') \\ &= 0. \end{aligned} \tag{A.10}$$

Similarly, the normally ordered covariance of creation and annihilation operators is

$$\begin{aligned} \left\langle a^\dagger(\omega)\,,\, a(\omega')\right\rangle &= \left\langle \alpha \left|a^\dagger(\omega)\, a(\omega')\right| \alpha\right\rangle - \left\langle \alpha \left|a^\dagger(\omega)\right| \alpha\right\rangle \langle \alpha |a(\omega')| \alpha\rangle \\ &= \alpha^*(\omega)\,\alpha(\omega') - \alpha^*(\omega)\,\alpha(\omega') \\ &= 0. \end{aligned} \tag{A.11}$$

Using equations A.9 and A.10 we derive for the covariance of creation operators

$$\left\langle a^\dagger(\omega)\,,\, a^\dagger(\omega')\right\rangle = \langle a(\omega)\,,\, a(\omega')\rangle^* = 0. \tag{A.12}$$

For the antinormally ordered covariance of annihilation and creation operators we calculate by using equations A.8 and A.11

$$\begin{aligned} \left\langle a(\omega)\,,\, a^\dagger(\omega')\right\rangle &= \left\langle \left[a(\omega)\,,\, a^\dagger(\omega')\right]\right\rangle + \left\langle a^\dagger(\omega)\,,\, a(\omega')\right\rangle \\ &= \delta(\omega - \omega') + 0 \\ &= \delta(\omega - \omega') . \end{aligned} \tag{A.13}$$

Note that the antinormally ordered covariance as in equation A.13 is the only one which has a non-zero value.

Appendix B

Production of squeezed light

Although we are in the context of this thesis focusing onto the quantum properties of the OPO there are some classical features which must not be placed aside. Firstly, in section B.1 we show how to get from Langevin equation to the expression used to determine the passive losses of the cavity. Then we perform the classical analysis of the OPO with the goal to determine the value of the threshold (section B.2). Finally in section B.3 we give the classical description of the parametric gain.

B.1 Losses in the cavity

The expression for the losses in the optical cavity can be found using the equation 1.9. Following the calculation shown in 1.3 up to the equation 1.15 we take now the pump power to be zero. In the absence of the the pump there will be no parametric oscillation. This situation is equal to seeding nothing more than the coherent field resonant to the cavity. Applying the boundary condition 1.18 one reaches

$$\begin{aligned}\tilde{a}_{out}(\omega) &= 2k_1\tilde{a}_{in}(\omega)(k_1+k_2-i\omega)^{-1} - \tilde{a}_{in}(\omega) = \\ &= (k_1-k_2+i\omega)(k_1+k_2-i\omega)^{-1}\tilde{a}_{in}(\omega)\end{aligned} \tag{B.1}$$

$$\frac{\tilde{a}_{out}(\omega)}{\tilde{a}_{in}(\omega)} = (k_1-k_2+i\omega)(k_1+k_2-i\omega)^{-1} \tag{B.2}$$

$$R = Re\left(\frac{\tilde{a}_{out}(\omega)}{\tilde{a}_{in}(\omega)}\right) = \sqrt{\frac{P_{out}}{P_{in}}} \tag{B.3}$$

$$R = \frac{T_1 - T_2}{T_1 + T_2} \tag{B.4}$$

$$T_2 = T_1 \cdot \frac{1-R}{1+R}. \tag{B.5}$$

B.2 Threshold value

The Hamiltonian 1.12 given in chapter 1 consists of two terms: the first term describes the energy of photons inside the cavity and the second term models the non-linear interaction induced by the pump field. In order to derive the threshold of the OPO, we will write the second (nonlinear interaction) term in the following form

$$H_{ni} = i\hbar g\left(\beta\left(a^{\dagger}\right)^{2} - \beta^{\dagger}a^{2}\right) \tag{B.6}$$

where we separate the previously used nonlinear coupling ε into the product of the pump field amplitude β and a coupling constant g. Since this calculation deals with a classical process we can use the Langevin equation of the OPO cavity in its classical form (here already writte in rotating reference frame)

$$\dot{\alpha} = -\left(k_1 + k_2\right)\alpha + g\beta\alpha^{*} + \sqrt{2k_1}\alpha_1^{in} + \sqrt{2k_2}\alpha_2^{in} \tag{B.7}$$

where $\alpha$and $\alpha^{*}$are cavity field amplitude and its complex-conjugate, β and β^{*} pump field amplitude driving the nonlinear interaction and its complex conjugate, α_1^{in} and α_2^{in} are the amplitudes of the field entering the cavity, and k_1 and k_2 denote the loss rates. One can write a similar equation for the pump field under the assumption that it is also resonant to one cavity mode.

$$\dot{\beta} = -k_3\beta - \frac{1}{2}g\alpha^{2} + \sqrt{2k_3}\beta^{in} \tag{B.8}$$

where k_3 is the loss rate of the blue pump field from the cavity.

For the threshold calculation α_1^{in}=α_2^{in}, are set to zero. Integrating the equation B.7 over one round trip in the cavity we obtain

$$\begin{bmatrix} \alpha\left(l\right) - \alpha\left(0\right) \\ \alpha^{*}\left(l\right) - \alpha^{*}\left(0\right) \end{bmatrix} = -\begin{bmatrix} \bar{k} & -\bar{g}\beta \\ -\bar{g}\beta^{*} & \bar{k} \end{bmatrix}\begin{bmatrix} \alpha\left(0\right) \\ \alpha^{*}\left(0\right) \end{bmatrix} \tag{B.9}$$

where $\bar{k} = k\Delta^{-1}$is the scaled loss rate and $\bar{g} = g\Delta^{-1}$ is the scaled coupling constant with the total loss rate being $k = k_1 + k_2$ and the free spectral range being $\Delta = cl^{-1}$. In addition, we assume that the cavity has a high finesse $F = \pi\bar{k}^{-1} \gg 1$.

Above the threshold the system is in a steady state so that the field amplitude, α, does not change after a round trip in the cavity. Therefore, the left side of the equation B.9 is equal to zero,

$$0 = \begin{bmatrix} \bar{k} & -\bar{g}\beta \\ -\bar{g}\beta^{*} & \bar{k} \end{bmatrix}\begin{bmatrix} \alpha\left(0\right) \\ \alpha^{*}\left(0\right) \end{bmatrix}. \tag{B.10}$$

For a nontrivial solution the parameters of the equation must fullfil the equation

$$\left|\beta_{th}\right|^{2} \equiv \left|\beta\right|^{2} = \bar{k}^{2}\bar{g}^{-2}. \tag{B.11}$$

This relation defines the pump power necessary for reaching the threshold. It is proportional to the ratio of loss rate to nonlinear coupling coefficient. The loss rate k is related to the cavity parameters through the following equation

$$2k = cl^{-1}\left(T_1 + T_2\right) = \Delta\left(T_1 + T_2\right). \tag{B.12}$$

The scaled nonlinear coupling coefficient can be also related to a measurable cavity parameter – the single pass nonlinearity E_{NL}. The single pass nonlinearity is defined as $E_{NL} = P_\beta P_\alpha^{-2}$, i.e. the blue power, P_β, generated from the crystal when only red light with power, P_α, is entering the cavity. The relation can be derived from equation B.8. To model a single pass setup we set $\beta_{in} = 0$ and $k_3 = 0$ yielding

$$\dot{\beta} = -\frac{1}{2} g \alpha^2. \tag{B.13}$$

Formaly integrating the equation B.13 for a single pass through the crystal one gets $c l_c^{-1} \left(\beta\left(l_c\right) - \beta\left(0\right)\right) = -\frac{1}{2} g \alpha^2$ or

$$\beta\left(l_c\right) \alpha^{-2} = -\bar{g}/2. \tag{B.14}$$

The power values can be calculated from the fields (here for α) by

$$P_\alpha = \Delta \hbar \omega_\beta \left|\alpha\right|^2. \tag{B.15}$$

By using the equation B.15 one can write

$$E_{NL} = \frac{P_\beta}{P_\alpha^2} = \frac{\bar{g}^2}{\Delta \hbar \omega_\beta}. \tag{B.16}$$

From this the threshold power can be calculated using the equation B.11

$$P_\beta^{th} = \Delta \hbar \omega_\beta \left|\beta_{th}\right|^2 = \Delta \hbar \omega_\beta \frac{\overline{k}^2}{\overline{g}^2}. \tag{B.17}$$

And finally combining the equations B.16, B.17 and B.12 one gets

$$P_\beta^{th} = \frac{\overline{k}^2}{E_{NL}} = \frac{\Delta^2 \left(T_1 + T_2\right)^2}{4 \Delta^2 E_{NL}} = \frac{\left(T_1 + T_2\right)^2}{4 E_{NL}}. \tag{B.18}$$

B.3 Parametric gain

In chapter 1 we have described theoretically the amplification and deamplification of the vacuum fluctuations in an OPO. Here we will show the classical theory of the parametric amplification. Since parametric amplification is in principal a classical process the calculation can start from equation B.7 for steady state while leaving one input field being non zero.

$$0 = -k\alpha + g\beta\alpha^* + \sqrt{2k_2}\alpha_1^{in}. \tag{B.19}$$

The parameter μ represents the the ratio of the pump field used in the experiment and the pump field necessary for reaching the threshold

$$\mu = \sqrt{\frac{P_\beta}{P_\beta^{th}}}. \tag{B.20}$$

Combining the equations B.20 and B.11 we obtain $k\mu = \beta g$. Using this we can write the equation B.19 and its complex-conjugate in the following way

$$k \begin{bmatrix} 1 & -\mu \\ -\mu & 1 \end{bmatrix} \begin{bmatrix} \alpha \\ \alpha^* \end{bmatrix} = \sqrt{2k_1} \begin{bmatrix} \alpha_1^{in} \\ \alpha_1^{in*} \end{bmatrix}. \tag{B.21}$$

Using the input-output relations 1.18 we obtain

$$\begin{bmatrix} \alpha_{out} \\ \alpha_{out}^* \end{bmatrix} = \frac{\sqrt{2k_1k_2}}{k\left(1-\mu^2\right)} \begin{bmatrix} 1 & \mu \\ \mu & 1 \end{bmatrix} \begin{bmatrix} \alpha_1^{in} \\ \alpha_1^{in*} \end{bmatrix}. \tag{B.22}$$

If we write the input field α_1^{in} that is seeded into the cavity as $\alpha_1^{in} = \left|\alpha_1^{in}\right| e^{i\rho}$, where ρ is the relative phase of this input field with respect to the pump field, we get

$$\alpha_{out} = \frac{\sqrt{2k_1k_2}}{k\left(1-\mu^2\right)} \left(\left|\alpha_1^{in}\right| e^{i\rho} + \mu \left|\alpha_1^{in}\right| e^{-i\rho}\right), \tag{B.23}$$

$$\frac{\alpha_{out}}{\left|\alpha_1^{in}\right|} = \frac{\sqrt{2k_1k_2}}{k\left(1-\mu^2\right)} \left(\left(1+\mu\right)\cos\rho + i\left(1-\mu\right)\sin\rho\right). \tag{B.24}$$

Or expressed in terms of power as it will be detected on a photodiode

$$V(\mu,\rho) = \frac{P_{out}}{P_1^{in}} = \frac{4k_1k_2}{k^2} \left[\frac{\cos^2\rho}{\left|1-\mu\right|^2} + \frac{\sin^2\rho}{\left|1+\mu\right|^2}\right]. \tag{B.25}$$

In this equation it is clearly visible that the seed light is amplified or attenuated depending on it's relative phase, ρ, to the pump field. For $\rho \approx 0$ the first term in the brackets is relevant and since it is larger than one causes an amplification of light. On the other hand, for $\rho \approx \frac{\pi}{2}$ the second term dominates, smaller than one and therefore attenuates the light.

Appendix C

Compensation of the diode-laser noise

In the first section C.1 we give the intermediate steps of the quantum calculation of the squeezing spectrum in the quasi-stationary regime. Afterwards in section C.2 we derive the classical theory of the delay in the cavity. In the chapter 3 this delay was used to determine the delay of the doubling cavity.

C.1 Quasi-stationary theory of squeezing

After inserting the Hamiltonian (equation 3.3 in the main text) Langevin equation of the OPO cavity (equation 3.2 in the main text) we obtain the following expression:

$$\dot{a} = -i\omega_0 a + \varepsilon e^{-i\omega_p t} a^\dagger - (k_1 + k_2)\, a + \sqrt{2k_1} a_{v1} + \sqrt{2k_2} a_{v2}. \tag{C.1}$$

We then apply the tranformation to rotating reference frame,

$$a = \widetilde{a} e^{-i\omega_0 t} \tag{C.2}$$

shifting the zero of the energy scale to the value of $\hbar\omega_0$. This transformation is applied on all the operators both on the left and the right side of the equation.

$$\dot{\widetilde{a}} = \varepsilon e^{-i(\omega_p - 2\omega_0)t} \tilde{a}^\dagger - (k_1 + k_2)\, \tilde{a} + \sqrt{2k_1} \tilde{a}_{v1} + \sqrt{2k_2} \tilde{a}_{v2}. \tag{C.3}$$

Assuming that the squeezed mode is detuned from the cavity resonance by $\omega_p - 2\omega_0 = 2\Delta\omega$ we can now apply the Fourier transform. As given in appendix A.1 the Fourier transform definition we use throughout this theses is given as

$$F\left[a\left(t\right)\right] = a\left(\omega\right), \tag{C.4}$$

$$\frac{1}{\sqrt{2\pi}} \int dt\, e^{i\omega t}\, a\left(t\right) = a\left(\omega\right) \longleftrightarrow a\left(t\right) = \frac{1}{\sqrt{2\pi}} \int dt\, e^{-i\omega t}\, a\left(\omega\right). \tag{C.5}$$

We solve the left side of the equation in the following way

$$\frac{1}{\sqrt{2\pi}}\int dt\, e^{i\omega t}\dot{\tilde{a}} = \left[\tilde{a}e^{i\omega t}\right]|_{-\infty}^{\infty} - \frac{1}{\sqrt{2\pi}}\int dt\, \tilde{a}\, i\omega e^{i\omega t} = -\frac{i\omega}{\sqrt{2\pi}}\int dt\, \tilde{a}e^{i\omega t}.$$

Finally we obtain the equation 3.6

$$\begin{aligned} -i\omega\tilde{a}(\omega) &= \varepsilon\tilde{a}^{\dagger}(-\omega+2\Delta\omega) - (k_1+k_2)\,\tilde{a}(\omega) \\ &\quad +\sqrt{2k_1}\tilde{a}_{v1}(\omega) + \sqrt{2k_2}\tilde{a}_{v2}(\omega). \end{aligned} \tag{C.6}$$

After shifting the frequency $\omega \to \omega + \Delta\omega$, we write the equation 3.6 and its Hermitian conjugate:

$$\begin{aligned} -i(\omega+\Delta\omega)\,\tilde{a}(\omega+\Delta\omega) &= \varepsilon\tilde{a}^{\dagger}(-\omega+\Delta\omega) - (k_1+k_2)\,\tilde{a}(\omega+\Delta\omega) \\ &+ \sqrt{2k_1}\tilde{a}_{v1}(\omega+\Delta\omega) + \sqrt{2k_2}\tilde{a}_{v2}(\omega+\Delta\omega), \end{aligned} \tag{C.7}$$

$$\begin{aligned} i(\omega+\Delta\omega)\,\tilde{a}^{\dagger}(\omega+\Delta\omega) &= \varepsilon^{*}\tilde{a}(-\omega+\Delta\omega) - (k_1+k_2)\,\tilde{a}^{\dagger}(\omega+\Delta\omega) \\ &+ \sqrt{2k_1}\tilde{a}_{v1}^{\dagger}(\omega+\Delta\omega) + \sqrt{2k_2}\tilde{a}_{v2}^{\dagger}(\omega+\Delta\omega). \end{aligned} \tag{C.8}$$

In the complex conjugate equation C.8 we exchange ω for $-\omega$, and solve it for $\tilde{a}^{\dagger}(-\omega+\Delta\omega)$:

$$\tilde{a}^{\dagger}(-\omega+\Delta\omega) = \frac{\varepsilon^{*}\tilde{a}(\omega+\Delta\omega) + \sqrt{2k_1}\tilde{a}_{v1}^{\dagger}(-\omega+\Delta\omega) + \sqrt{2k_2}\tilde{a}_{v2}^{\dagger}(-\omega+\Delta\omega)}{[i(-\omega+\Delta\omega)+(k_1+k_2)]}. \tag{C.9}$$

This solution allows us to eliminate $\tilde{a}^{\dagger}(-\omega+\Delta\omega)$ in equation C.7 and then to solve for the field inside the cavity $\tilde{a}(\omega+\Delta\omega)$:

$$\begin{aligned} \tilde{a}(\omega+\Delta\omega) &= \varepsilon\left(\sqrt{2k_1}\tilde{a}_{v1}^{\dagger}(-\omega+\Delta\omega) + \sqrt{2k_2}\tilde{a}_{v2}^{\dagger}(-\omega+\Delta\omega)\right)X^{-1} \\ &\quad +\sqrt{2k_1}\tilde{a}_{v1}(\omega+\Delta\omega)\,[i(-\omega+\Delta\omega)+(k_1+k_2)]\,X^{-1} \\ &\quad +\sqrt{2k_2}\tilde{a}_{v2}(\omega+\Delta\omega)\,[i(-\omega+\Delta\omega)+(k_1+k_2)]\,X^{-1} \end{aligned} \tag{C.10}$$

where

$$X = ((k_1+k_2)-i\omega)^2 + \Delta\omega^2 - |\varepsilon|^2. \tag{C.11}$$

Using the input-output relation 3.8 we reach the output field (Bogoliubov transformation from input to output fields)

$$\begin{aligned} \tilde{a}_{out}(\omega+\Delta\omega) &= g_5\tilde{a}_{v1}(\omega+\Delta\omega) + g_6\tilde{a}_{v1}^{\dagger}(-\omega+\Delta\omega) + \\ &\quad g_7\tilde{a}_{v2}(\omega+\Delta\omega) + g_8\tilde{a}_{v2}^{\dagger}(-\omega+\Delta\omega) \end{aligned} \tag{C.12}$$

where

$$g_5 = \left(k_1^2 - (k_2 - i\omega)^2 + \Delta\omega\,(2k_1 i - \Delta\omega) + |\varepsilon|^2\right) X^{-1} \quad \text{(C.13)}$$

$$g_6 = 2\varepsilon k_1 X^{-1} \quad \text{(C.14)}$$

$$g_7 = 2\sqrt{k_1 k_2}\,(i\,(-\omega + \Delta\omega) + (k_1 + k_2))\,X^{-1} \quad \text{(C.15)}$$

$$g_8 = 2\varepsilon X^{-1}\sqrt{k_1 k_2}. \quad \text{(C.16)}$$

As in the calculation in section 1.3 from now on all frequencies and rates are scaled to the cavity linewidth $\delta\nu = k_1 + k_2$. The parameters we use are the same as there: $\Omega = \omega\,(k_1 + k_2)^{-1}$, $\eta = k_1\,(k_1 + k_2)^{-1}$, $1 - \eta = k_2\,(k_1 + k_2)^{-1}$, $\mu = \varepsilon\,(k_1 + k_2)^{-1}$. The output field expressed in these parameters is given in equation 3.9.

To reach the squeezing function we write the output field in the same manner as in section 1.3 - in terms of phase quadratures. The squeezing function is expressed by the covariance whose only non-zero terms are the anti-normally ordered ones. In the appendix A.2 we calculate the normally (equal to zero) and anti-normally ordered terms of the covariance.

C.2 Cavity delay

Here we will show the calculation of the delay introduced by a linear cavity. First, we derive the transmission of the cavity as depicted in figure C.1

We start with a monochromatic incoming field E_{in},

$$E_{in} = E_0 e^{i\omega t}. \quad \text{(C.17)}$$

The electrical field directly behind the first mirror can be expressed by the circulating field E_4 and the incoming field E_{in} as

$$E_1 = tE_{in} - rE_4 \quad \text{(C.18)}$$

where r and t are reflection and transmission coefficients, respectively.

The field E_2 in front of the second mirror is equal to the the field E_1 with a phase factor due to the propagation over the length d (the length of the cavity)

$$E_2 = E_1 e^{ikd}. \quad \text{(C.19)}$$

The reflected field E_3 will suffer the phase shift of $\pi$with respect to the field E_2

$$E_3 = -rE_2. \quad \text{(C.20)}$$

Finally, we we can write the electric field E_4 expressing it as a function of the electric field E_1

$$E_4 = E_3 e^{ikd} = -rE_2 e^{ikd} = -rE_1 e^{2ikd}. \quad \text{(C.21)}$$

Exchanging E_4 in the equation C.18 for the field E_1 we obtain

$$E_1 = tE_{in} + r^2 E_1 e^{2ikd} \quad \text{(C.22)}$$

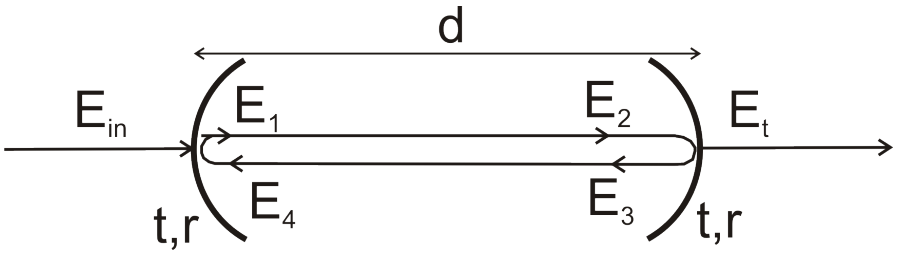

Figure C.1: Schematic of a linear cavity of the length d made of spherical mirrors with the reflection coefficient r and transmission coefficient t.

$$E_1 = \frac{t}{1 - r^2 e^{2ikd}} E_{in}. \tag{C.23}$$

The field transmitted through the cavity has the form

$$E_t = tE_1 e^{ikd} = \frac{t^2 e^{ikd}}{1 - r^2 e^{2ikd}} E_{in} = \frac{t^2 e^{ikd}}{1 - r^2 e^{2ikd}} E_0 e^{i\omega t}. \tag{C.24}$$

The transmitted field can be also written in terms of the transfer function $K(\omega)$

$$E_t = K(\omega) E_0 e^{i\omega t} = K_0 e^{i\varphi} E_0 e^{i\omega t}. \tag{C.25}$$

This transfer function can be separated into product of the amplitude (K_0) and the phase (φ) part

$$\begin{aligned} K_0 e^{i\varphi} &= \frac{t^2 e^{ikd}}{1 - r^2 e^{2ikd}} \\ &= \frac{t^2 e^{i\omega dc^{-1}}}{1 - r^2 e^{2i\omega dc^{-1}}} \times \frac{1 - r^2 e^{-2i\omega dc^{-1}}}{1 - r^2 e^{-2i\omega dc^{-1}}} \\ &= \frac{t^2 \left(e^{i\omega dc^{-1}} - r^2 e^{-i\omega dc^{-1}} \right)}{1 + r^4 - 2r^2 \cos\left(2\omega dc^{-1}\right)}. \end{aligned} \tag{C.26}$$

If we simplify the previous formula we can also separate the amplitude and the phase of the transfer function on the right side

$$\begin{aligned} K_0 \left(\cos\varphi + i\sin\varphi\right) &= \left(\left(1 - r^2\right) \cos\left(\omega dc^{-1}\right) + i \left(1 + r^2\right) \sin\left(\omega dc^{-1}\right) \right) \\ &\times \frac{t^2}{1 + r^4 - 2r^2 \cos\left(2\omega dc^{-1}\right)} \end{aligned} \tag{C.27}$$

which enables us to solve the equation for the phase induced by the cavity

$$\tan\varphi = \frac{\sin\varphi}{\cos\varphi} = \frac{\sin\left(\omega dc^{-1}\right)\left(1 + r^2\right)}{\cos\left(\omega dc^{-1}\right)\left(1 - r^2\right)} \tag{C.28}$$

$$\varphi = \arctan\left(\tan\left(\frac{\omega d}{c} \right) \frac{\left(1 + r^2\right)}{\left(1 - r^2\right)} \right). \tag{C.29}$$

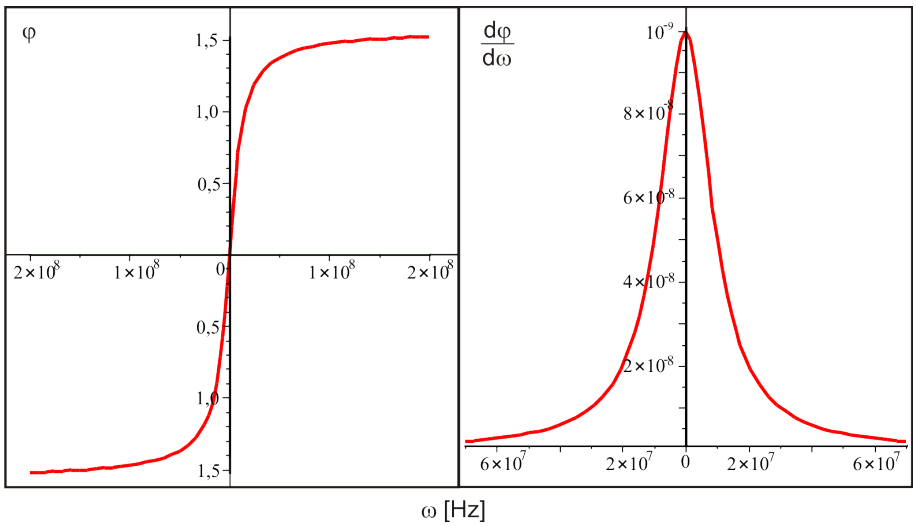

Figure C.2: Phase φ and group delay $\frac{d\varphi}{d\omega}$ of a cavity of lenght $d = 30\,\mathrm{cm}$ and $r = 0.99$.

The group delay of the cavity can then be calculated from the phase of the cavity as

$$\tau_g = \frac{d\varphi}{d\omega} = \frac{d}{c} \times \frac{\left(1 - r^4\right)}{\left(1 + r^2\right)^2 - 4r^2 \cos^2\left(\omega d c^{-1}\right)}. \tag{C.30}$$

For the resonance condition $\omega = 0$ we obtain the following formulas

$$\cos\left(\omega d c^{-1}\right) = 1, \tag{C.31}$$

$$\tau_g = \left.\frac{d\varphi}{d\omega}\right|_{resonance} = \frac{d}{c} \times \frac{1 - r^4}{\left(1 - r^2\right)^2} \cong \frac{1}{\pi \delta \nu}. \tag{C.32}$$

Bibliography

[1] D. Akamatsu, K. Akiba, and M. Kozuma. *Phys. Rev. Lett.*, 92(20):203602, 2004.

[2] J. Appel, F Figueroa, D. Korystov, M. Lobino, and Lvovsky A. I. *Physical Review Letters*, 100(9):093602, 2008.

[3] A Arie. In *Lecture notes, Q&NLO2006 Summer school*, 2006.

[4] J. A. Armstrong, N. Bloembergen, J. Ducuing, and P. S. Pershan. *Phys. Rev.*, 127(6):1918–1939, 1962.

[5] K. J. Aström and T. Hägglund. *Advanced PID Control*. ISA, 2004.

[6] H-A Bachor and T.C. Ralf. *A Guide to Experiments in Quantum Optics*. WILEY-VCH, 2004.

[7] E.D. Black. *American Journal of Physics*, 69:79–87, 2000.

[8] B. Boulanger, M.M. Fejer, R. Blachman, and Bordui P.F. *Applied Physics Letters*, 65(19):2401–2403, 1994.

[9] B. Boulanger, J.-P. Fève, and Y. Guillien. *Opt. Lett.*, 25(7):484–486, 2000.

[10] B. Boulanger, I. Rousseau, J.-P. Fève, M. Maglione, B. Menaert, and G. Marnier. *IEEE JOURNAL OF QUANTUM ELECTRONICS*, 35:281, 1999.

[11] W.P. Bowen. *Experiments towards a Quantum Information Network with Squeezed Light and Entanglement*. PhD thesis, University of Otago, 2003.

[12] G.D. Boyd and D.A. Kleiman. *J.Appl.Phys.*, 39:3597, 1968.

[13] C.M. Caves. *Phys. Rev. D*, 23(8):1693–1708, 1981.

[14] C.M. Caves. *Phys. Rev. D*, 26(8):1817–1839, 1982.

[15] C.M. Caves and B.L. Schumaker. *Phys. Rev. A*, 31(5):3068–3092, 1985.

[16] M. J. Collett and C. W. Gardiner. *Phys. Rev. A*, 30(3):1386–1391, 1984.

[17] L.-M. Duan, M. D. Lukin, J. I. Cirac, and P. Zoller. *Nature*, 414(6862):413–418, 2001.

[18] R.C. Eckardt, H. Masuda, Y.X. Fan, and R.L. Byer. *Quantum Electronics, IEEE Journal of*, 26(5):922–933, 1990.

[19] G. J. Edwards, M. P. Scripsick, L. E. Halliburton, and R. F. Belt. *Phys. Rev. B*, 48(10):6884–6891, 1993.

[20] M.W. Fleming and A. Mooradian. *Applied Physics Letters*, 38(7):511–513, 1981.

[21] P. A. Franken and J. F. Ward. *Rev. Mod. Phys.*, 35(1):23–39, 1963.

[22] C. W. Gardiner and P. Zoller. *Quantum Noise*. Springer Verlag, 2000.

[23] P. Grangier, R. E. Slusher, B. Yurke, and A. LaPorta. *Phys. Rev. Lett.*, 59(19):2153–2156, 1987.

[24] K. Hammerer, A.S. Sörensen, and E.S. Polzik. 2008.

[25] G. Hansson, H. Karlsson, S. Wang, and F. Laurell. *Appl. Opt.*, 39(27):5058–5069, 2000.

[26] H. Hellwig, J. Liebertz, and L. Bohatý. *Solid State Communications*, 109(4):249 – 251, 1998.

[27] H. Hellwig, J. Liebertz, and L. Bohatý. *Journal of Applied Physics*, 88(1):240–244, 2000.

[28] C. Henry. *IEEE JOURNAL OF QUANTUM ELECTRONICS*, 18:259, 1982.

[29] C. Henry. *Lightwave Technology, Journal of*, 4(3):298–311, 1986.

[30] G. Hètet, B.C. Buchler, O. Glöeckl, T.M.L. Hsu, A.M. Akulshin, H.-A. Bachor, and P.K. Lam. *Opt. Express*, 16(10):7369–7381, 2008.

[31] K. Honda, D. Akamatsu, M. Arikawa, Y. Yokoi, K. Akiba, S. Nagatsuka, T. Tanimura, A. Furusawa, and M. Kozuma. *Physical Review Letters*, 100(9):093601, 2008.

[32] D. B. Horoshko and S. Ya. Kilin. *Phys. Rev. A*, 61(3):032304, 2000.

[33] M. T. L. Hsu, G. Hétet, O. Glöckl, J.J. Longdell, B.C. Buchler, H.-A. Bachor, and P.K. Lam. *Physical Review Letters*, 97(18):183601, 2006.

[34] G. Hétet, O. Glöckl, K.A. Pilypas, C.C. Harb, B.C. Buchler, H.-A. Bachor, and P.K. Lam. *Journal of Physics B: Atomic, Molecular and Optical Physics,*, 40:221, 2007.

[35] T. Kanada and K. Nawata. *IEEE JOURNAL OF QUANTUM ELECTRONICS*, 15:559, 1979.

[36] H. Karlsson. *Fabrication of periodically poled crystals from the KTP family and their applications in nonlinear optics*. PhD thesis, 1999.

[37] C. Koch. *PTB-Bericht Opt-43, Physikalisch-Technische Bundesanstalt, Braunschweig*, 1994.

[38] H. Kogelnik and T. Li. *Appl. Opt.*, 5(10):1550, 1966.

[39] A. Kuzmich, Klaus Mølmer, and E. S. Polzik. *Phys. Rev. Lett.*, 79(24):4782–4785, 1997.

[40] M. Lax. *Rev. Mod. Phys.*, 38(3):541–566, 1966.

[41] M. Lax. *Phys. Rev.*, 160(2):290–307, 1967.

[42] R. Le Targat, J.-J. Zondy, and P. Lemonde. *Optics Communications*, 247:471–481, 2005.

[43] J. Liu, X. He, J. Xu, G. Zhou, S. Zhou, G. Zhao, and S. Li. *Journal of Crystal Growth*, 260(3-4):486 – 489, 2004.

[44] L. Mandel and E. Wolf. *Optical Coherence and Quantum Optics*. Cambridge University Press, 1995.

[45] G. Milburn and D. F. Walls. *Optics Communications*, 11:401, 1981.

[46] P.W. Milonni and J.H. Eberly. *Lasers*. Wiley and Sons, 1988.

[47] S. Motokoshi, T. Jitsuno, Y. Izawa, and M. Nakatsuka. 2001.

[48] M. Nakamura, K. Aiki, N. Chinone, R. Ito, and J. Umeda. *Journal of Applied Physics*, 49(9):4644–4648, 1978.

[49] K. Ogata. *Modern Control Engineering*. Prentice Hall; 3 Sub edition, 1996.

[50] Z.Y. Ou, C.K. Hong, and L. Mandel. *J. Opt. Soc. Am. B*, 4, 1987.

[51] M.V. Pack, D.J. Armstrong, and A.V. Smith. *J. Opt. Soc. Am. B*, 20(10):2109–2116, 2003.

[52] T.L. Paoli. *Applied Physics Letters*, 24(4):187–190, 1974.

[53] E. S. Polzik, J. Carri, and H. J. Kimble. *Applied Physics B: Lasers and Optics*, 55:279, 1992.

[54] F. Riehle. *Frequency Standards*. Wiley-VCH Verlag, Weinheim, 2004.

[55] D.A. Roberts. *Quantum Electronics, IEEE Journal of*, 28(10):2057–2074, 1992.

[56] E.A. Saleh and M.C. Teich. *Fundamentals of photonics*. John Wiley & Sons, Inc., 1991.

[57] A. L. Schawlow and C. H. Townes. *Phys. Rev.*, 112(6):1940–1949, 1958.

[58] K. Schneider, M. Lang, J. Mlynek, and S Schiller. *OPTICS EXPRESS*, 2:61, 1998.

[59] C Schori, J.L. Sörensen, and E.S. Polzik. *PHYSICAL REVIEW A*, 66:033802, 2002.

[60] B.L. Schumaker and C.M. Caves. *Phys. Rev. A*, 31(5):3093–3111, 1985.

[61] M.O. Scully and M.S. Zubairy. *Quantum Optics*. Cambridge University Press, 1997.

[62] J.F. Sherson, H. Krauter, R.K. Olsson, B. Julsgaard, K. Hammerer, I. Cirac, and E.S. Polzik. *Nature*, 443(7111):557–560, 2006.

[63] R. E. Slusher, P. Grangier, A. LaPorta, B. Yurke, and M. J. Potasek. *Phys. Rev. Lett.*, 59(22):2566–2569, 1987.

[64] R. E. Slusher, L. W. Hollberg, B. Yurke, J. C. Mertz, and J. F. Valley. *Phys. Rev. Lett.*, 55(22):2409–2412, 1985.

[65] D.A. Steck. Rubidium 87 d line data.

[66] Y. Takeno, M. Yukawa, H. Yonezawa, and A. Furusawa. *Opt. Express*, 15(7):4321–4327, 2007.

[67] T. Tanimura, D. Akamatsu, Y. Yokoi, A. Furusawa, and M. Kozuma. *Opt. Lett.*, 31(15):2344–2346, 2006.

[68] F. Torabi-Goudarzi and E. Riis. *Optics Communications*, 227:389–403, 2003.

[69] J.K. Tyminski. *Journal of Applied Physics*, 70, 1991.

[70] H. Vahlbruch, M. Mehmet, S. Chelkowski, B. Hage, A. Franzen, N. Lastzka, S. Goß ler, K. Danzmann, and R. Schnabel. *Physical Review Letters*, 100(3):033602, 2008.

[71] H. Vanherzeele, J.D. Bierlein, and F.C. Zumsteg. *Appl. Opt.*, 27(16):3314–3316, 1988.

[72] M. Davis L. Huang C. Velsko, S.P. Webb. *IEEE JOURNAL OF QUANTUM ELECTRONICS*, 27:2182–2192, 1991.

[73] D. F. Walls and G.J. Milburn. *Quntum Optics*. Springer Verlag, 1995.

[74] L.-A. Wu, H. J. Kimble, J. L. Hall, and H. Wu. *Phys. Rev. Lett.*, 57(20):2520–2523, 1986.

[75] M. Xiao, L.-A. Wu, and H. J. Kimble. *Phys. Rev. Lett.*, 59(3):278–281, 1987.

[76] Y. Yamamoto, S. Machida, and O. Nilsson. *Phys. Rev. A*, 34(5):4025–4042, 1986.

[77] B. Yurke. *Phys. Rev. A*, 29(1):408–410, 1984.